The Astrophysical Journal Supplement Series, 282:34 (18pp), 2026 February https://doi.org/10.3847/1538-4365/ae2a21
© 2026. The Author(s). Published by the American Astronomical Society.
OPEN ACCESS

A Pan-galaxy Study of Synthetic Giant Molecular Filaments: A Turbulence-dominated Life Cycle

Zipeng Hu[1,3], Ke Wang[1], Mark R. Krumholz[2], and Keyun Su[1]
[1] Kavli Institute for Astronomy and Astrophysics, Peking University, 5 Yiheyuan Road, Haidian District, Beijing 100871, People's Republic of China; zphu.charles@gmail.com, kwang.astro@pku.edu.cn
[2] Research School of Astronomy and Astrophysics, Australian National University, Canberra ACT 2601, Australia
Received 2025 October 8; revised 2025 December 2; accepted 2025 December 5; published 2026 January 16

Abstract

Recent surveys of the Galactic plane have revealed dozens of giant molecular filaments (GMFs), with lengths ranging from tens to hundreds of parsecs, yet their origins and life cycles remain debated. In this work, we analyze over 700 GMFs identified from synthetic CO emission maps of a high-resolution magnetohydrodynamic simulation of a Milky Way–like galaxy, whose lengths range from ∼10 to ∼300 pc. We find that turbulent shock from galactic shear and stellar feedback are the primary drivers of GMF formation. Magnetized turbulence dominates their internal dynamics, supporting the filaments against global collapse while simultaneously inducing fragmentation into dense clumps. This fragmentation follows the turbulence-driven sausage instability model, rather than pure Jeans instability, and triggers efficient star formation along the filaments. Cloud–cloud collisions are frequent, affecting more than 70% of GMFs, and often disrupt or reshape their morphology. The typical filamentary lifetime is $t_{\rm fil} = 14^{+2}_{-5}$ Myr, comparable to the crossing time of giant molecular clouds (GMCs). The molecular gas half-life is ∼7 Myr, similar to that of GMCs, indicating that GMFs are transient but dynamically important structures.

Unified Astronomy Thesaurus concepts: Interstellar clouds (834); Interstellar filaments (842); Star formation (1569)

Materials only available in the online version of record: animation

1. Introduction

Over the past two decades, high-resolution surveys with the Atacama Large Millimeter/submillimeter Array, JWST, Very Large Array, and Herschel have firmly established that the interstellar medium (ISM) in our Galaxy and nearby systems is organized into hierarchical networks of filamentary structures (e.g., P. André et al. 2010; D. Arzoumanian et al. 2011; P. André et al. 2014; K. Wang et al. 2015; A. Hacar et al. 2018; C. Li et al. 2021; D. M. Paré et al. 2024; T. Temim et al. 2024; K. Wang et al. 2024; Y. Jiang et al. 2025). These structures range from kiloparsec-long atomic filaments to subparsec dense fibers within molecular clouds (A. Hacar et al. 2022). This filamentary web serves as the primary nursery for star formation, connecting large-scale gas reservoirs to the dense clumps and cores where stars are born. Among these structures, giant molecular filaments (GMFs) represent the largest, high–aspect-ratio filaments (>10 pc) that are dense enough to host star formation. Since the discovery of Nessie (J. M. Jackson et al. 2010; A. A. Goodman et al. 2014), a ∼150 pc filament with an aspect ratio over 300:1, dozens of GMFs have been identified across the Galactic plane (S. E. Ragan et al. 2014; K. Wang et al. 2015; C. Zucker et al. 2015; J. Abreu-Vicente et al. 2016; K. Wang et al. 2016; Y. Ge & K. Wang 2022; Y. Ge et al. 2023; K. Wang et al. 2024). Owing to their large spatial extent and high masses, GMFs both connect galactic dynamics to star formation and contribute significantly to the Galactic star formation rate (SFR). Understanding their life cycle and the underlying physical mechanisms is therefore essential for developing a complete theory of star formation and galactic evolution, and has become increasingly timely with the advent of high-resolution GMF catalogs.

A central but unresolved question concerns which physical processes govern the life cycle of GMFs. Early studies of Nessie and a handful of other GMFs (A. A. Goodman et al. 2014; K. Wang et al. 2015; C. Zucker et al. 2015) reported strong associations with spiral arms, suggesting that GMFs form the "bones" of spiral arms and are shaped by the spiral gravitational potential throughout their evolution. However, other surveys find such associations less frequent (S. E. Ragan et al. 2014; C. Zucker et al. 2018; K. Wang et al. 2024), challenging the universality of this picture. Owing to their large sizes, GMFs are subject to a complex interplay of processes—including self-gravity, magnetic fields, turbulence, stellar feedback, and cloud–cloud collisions (CCC). The relative importance of each mechanism at different evolutionary stages remains uncertain. Statistical studies of the relative orientation between filament spines and magnetic fields have shown a tendency for alignment at low column densities, transitioning to preferentially perpendicular orientations at high column densities (Planck Collaboration et al. 2016; D. L. Jow et al. 2018). This transition, reported at $N \simeq 10^{21-22}\,{\rm cm}^{-2}$, has been interpreted as evidence that gas accretion flows are guided by magnetic fields during the early formation stage (J. D. Soler & P. Hennebelle 2017). However, using Planck data, K. Wang et al. (2024) reported a random distribution of relative orientations in a linear filament catalog

[3] Boya Fellow.

Original content from this work may be used under the terms of the Creative Commons Attribution 4.0 licence. Any further distribution of this work must maintain attribution to the author(s) and the title of the work, journal citation and DOI.

across the full Galactic plane, suggesting that multiple formation mechanisms may be at play. Achieving a clear picture of the GMF life cycle requires precise theoretical modeling that incorporates realistic galactic environments and physical processes.

Recent multiscale galactic simulations have begun to address this complexity (A. Duarte-Cabral & C. L. Dobbs 2017; C. Zucker et al. 2019; B. Zhao et al. 2024; R. Pillsworth et al. 2025), but several limitations remain. First, in those works, most GMF samples are extracted from kiloparsec-scale subregions, which may not capture the diversity of galactic environments. Second, synthetic GMFs are often identified directly from volume or column density thresholds applied to simulation data, creating a methodological gap with observations, which rely on 2D projections and specific tracers such as CO or dust emission. Finally, crucial physical mechanisms are often omitted. For example, C. Zucker et al. (2019) excluded self-gravity, magnetic fields, and stellar feedback, while A. Duarte-Cabral & C. L. Dobbs (2017) neglected magnetic fields altogether. None of these works included presupernova feedback such as photoionization, which can rapidly disperse GMCs before supernova explosions occur (M. Y. Grudić et al. 2018; J. M. D. Kruijssen et al. 2019; M. Chevance et al. 2023).

In this study, we overcome these limitations by analyzing a high-resolution magnetohydrodynamic (MHD) simulation of an entire Milky Way–like galaxy that incorporates a comprehensive stellar feedback model. We apply a filament identification algorithm directly to synthetic CO emission maps generated from the simulation, mirroring observational methodologies. This approach enables a robust and self-consistent investigation of the GMF life cycle within a realistic, dynamically evolving galactic environment.

This paper is organized as follows. In Section 2, we describe the simulation setup, the implementation of key physical mechanisms, the synthetic CO pipeline, and the GMF identification algorithm. In Section 3, we present the statistical properties of the simulated GMF population and compare them with observational catalogs. In Section 4, we analyze the full GMF life cycle, quantifying the roles of different physical mechanisms across evolutionary stages. In Section 5, we discuss how different GMF identification algorithms affect the GMF properties, and the difference between GMFs and nonfilamentary giant molecular clouds (GMCs). We summarize our findings in Section 6.

2. Methods

Section 2.1 describes the basic setup of our Milky Way–like galaxy simulation and the implementation of the key physical mechanisms in our numerical model. Section 2.2 summarizes the pipeline for generating synthetic CO emission maps, and Section 2.3 outlines the GMF identification algorithm.

2.1. Simulation

The numerical data analyzed in this study are drawn from the Milky Way–like galactic simulation of Z. Hu et al. (2024, hereafter H24). The simulation was performed with the GIZMO code, which employs a mesh-free, Lagrangian finite-mass Godunov method to solve the MHD equations (P. F. Hopkins 2015; P. F. Hopkins 2016; P. F. Hopkins & M. J. Raives 2016). Below, we provide a brief overview of the setup and numerical methods, and refer readers to H24 for full details. The initial conditions follow the "high-resolution" case of the AGORA project (J.-h. Kim et al. 2016), which includes a dark matter halo of mass $M_{\rm DM} = 1.07 \times 10^{12}\ M_\odot$, a stellar disk of mass $M_* = 3.4 \times 10^{10}\ M_\odot$, a bulge of mass $M_{\rm B} = 4.3 \times 10^9\ M_\odot$, and a gas disk of mass $M_{\rm gas} = 8.6 \times 10^9\ M_\odot$. Thus, the gas mass constitutes ∼20% of the total baryonic mass. The gas disk has a scale length of $R_0 = 3.43218$ kpc and a scale height of $z_0 = 0.343218$ kpc. The initial magnetic field of the simulated galaxy in cylindrical coordinates $(R,\ \phi,\ z)$ can be described as

$$B_R = 0, \tag{1}$$

$$B_\phi = B_0 \exp(-R/R_0) \exp(-|z|/z_0), \tag{2}$$

$$B_z = 0, \tag{3}$$

where $B_0 = 10\ \mu$G. The toroidal field geometry and the mean field strength are chosen to mimic the ordered component of the observed Galactic magnetic field (R. Beck 2015).

The simulation consists of two stages. In the first stage, it evolves for 0.7 Gyr at a gas mass resolution of $\Delta M_{\rm gas} = 859.3\ M_\odot$, allowing the galaxy to settle into a stable SFR of $\sim 3\ M_\odot\ {\rm yr}^{-1}$. At the end of this stage, all gas particles are split into 10 equal-mass particles, improving the mass resolution to $\sim 90\ M_\odot$. This corresponds to a Jeans length of ∼0.6 pc, which serves as the characteristic spatial resolution. The snapshot produced after this particle splitting becomes the initial condition of the second stage, which is run for 40 Myr—longer than the 23 Myr duration in H24—to ensure that the full life cycle of GMFs can be traced. This extension is motivated by previous studies, which report typical GMC lifetimes of ∼20 Myr (J. M. D. Kruijssen et al. 2019; M. Chevance et al. 2020). Snapshots are output every 1 Myr. For our analysis, we focus on the snapshot at $t = 720$ Myr, which provides a sufficient time window (20 Myr) both before and after for tracing GMF formation and subsequent evolution. In Figure 1, the face-on gas surface density of this snapshot is shown in the upper left panel, and the face-on magnetic field strength map is shown in the lower left panel. Previous galaxy simulation works show that the field strength would be amplified by turbulence and stellar feedback in the early stage of galaxy evolution, then reaches a steady state (e.g., E. Ntormousi 2018; H. Robinson et al. 2025), which would affect the star formation process and mass distribution within GMCs. Therefore, we plot the mass-weighted mean magnetic field strength in the second simulation stage against simulation time in the lower right panel of Figure 1, which confirms that the galactic magnetic field in this simulation stage has reached a steady state.

The GIZMO code incorporates a time-dependent chemical network for hydrogen and helium cooling, together with metal-line cooling computed from pretabulated CLOUDY models (G. J. Ferland et al. 1998) via the GRACKLE library (B. D. Smith et al. 2017). Star formation is modeled stochastically by converting gas particles into star particles once their density exceeds $\rho_{\rm crit} = 1000 m_{\rm H}\ {\rm cm}^{-3}$, with an efficiency per freefall time of $\epsilon_{\rm ff} = 0.01$. To limit computational expense, extremely dense gas ($\rho_{\rm g} > 100\rho_{\rm crit}$) is converted rapidly into stars by assigning $\epsilon_{\rm ff} = 1$. Because the stellar particle mass is only $\sim 89\ M_\odot$, too low to fully sample the initial mass function (IMF), stellar feedback is implemented stochastically. For each star particle, the stellar population synthesis code SLUG (R. L. da Silva et al. 2012; M. R. Krumholz et al. 2015) samples a unique stellar population from a Chabrier IMF (G. Chabrier 2005).

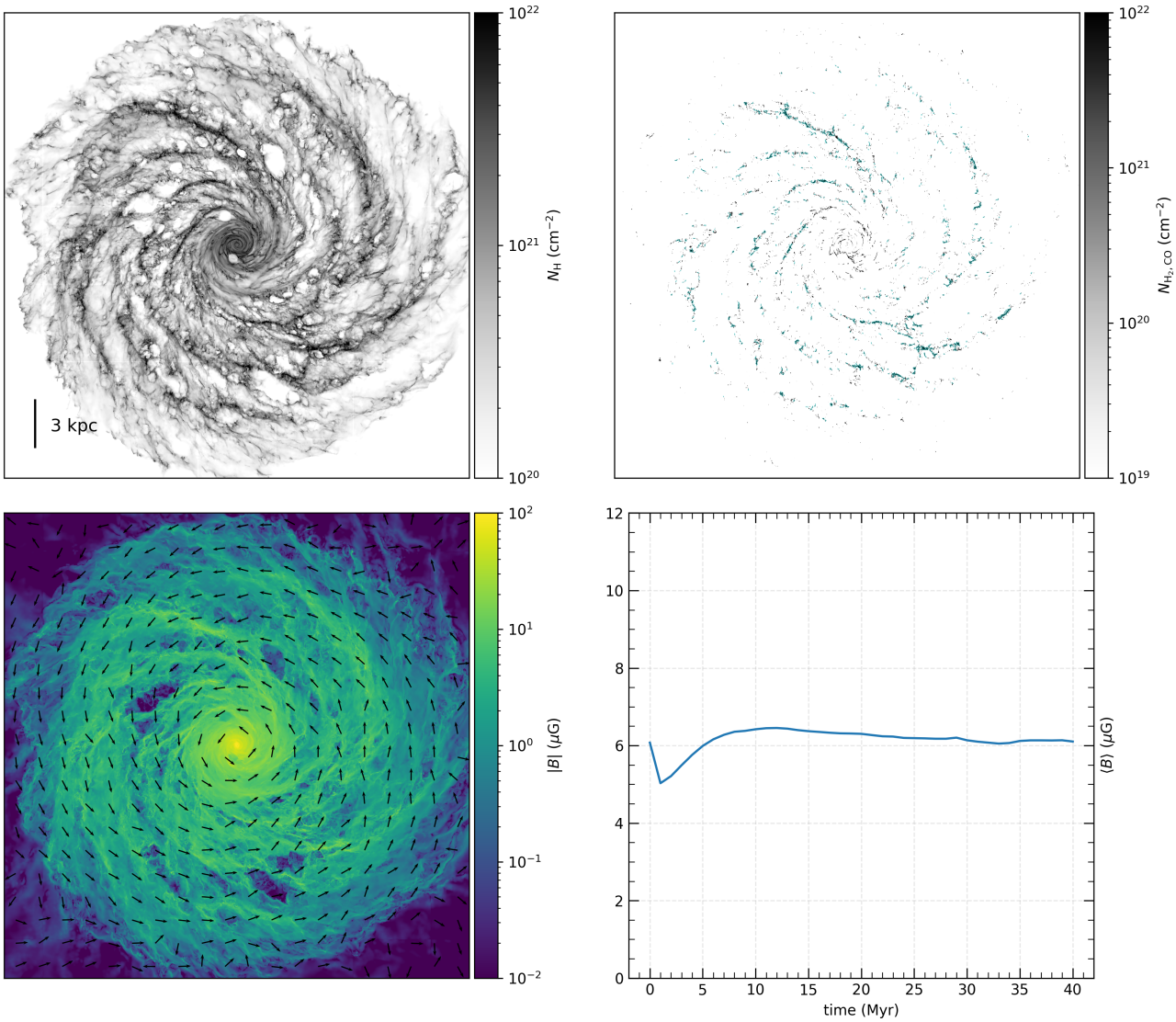

Figure 1. Milky Way–like spiral galaxy simulation at $t = 720$ Myr. Upper left: total gas column density map, where N_H is the total column density of H nuclei. Upper right: molecular hydrogen column density traced by synthetic CO $J = 1 \rightarrow 0$ emission. The cyan contours illustrate the positions of GMFs identified in Section 2.3. Each map covers 30×30 kpc with a pixel size of 1 pc. Lower left: mass-weighted B-field strength map. The green arrows indicate the local magnetic field directions in the x–y plane. Lower right: the mass-weighted mean magnetic field as a function of time in the second stage of this simulation.

We focus on two kinds of stellar feedback most relevant at parsec scales: Type II supernovae (SNe II) and photoionization. For SNe II, SLUG provides the number of events ($N_{\rm SNe\ II}$) and the total ejecta mass ($M_{\rm ej}$) at each time step. Assuming each event releases 10^{51} erg, we calculate the total ejected energy and momentum, which are then deposited into neighboring gas particles following the algorithm of P. F. Hopkins et al. (2018a, 2018b). For photoionization, we use a Strömgren volume method, whereby the ionizing luminosity from SLUG is used to sequentially heat the nearest nonionized ($T < 10^4$ K) gas particles to 10^4 K until the photon budget is exhausted. See H24 for full details on how SNe II and photoionization are implemented.

2.2. Synthetic Observation

To mimic how observers identify dense molecular structures, we generate synthetic CO emission observations of the entire simulated galaxy. We adopt the same algorithm as in H24, and therefore only provide a brief summary here. First, we post-process our simulation snapshots using the astrochemistry and radiative transfer code DESPOTIC (M. R. Krumholz 2014). This approach is computationally more efficient than performing on-the-fly chemistry calculations and has the important advantage that it captures non–local thermodynamic equilibrium excitation effects, which must be included in order to produce credible CO emission predictions. Using DESPOTIC, we precompute a look-up table of the ^{12}CO $J = 1 \rightarrow 0$ luminosity per hydrogen atom, $l_{\rm CO}$. The table spans a grid in the parameter space of three key local gas properties: hydrogen number density ($n_{\rm H} = 10^{-2}$–10^6 cm^{-3}), column density ($N_{\rm H} = 10^{19}$–10^{25} cm^{-2}), and velocity gradient ($dv/dr = 10^{-3}$–10^2 km s^{-1} pc^{-1}). The interstellar radiation field (ISRF) strength is assumed to be the solar neighborhood value throughout the computation.

For each gas particle in the simulation, we obtain $n_{\rm H}$ and dv/dr directly from the simulation outputs, while $N_{\rm H}$ is derived from the corresponding pixel in the face-on column density map shown in Figure 1 (upper left panel). We then determine

$l_{\rm CO}$ by performing a trilinear interpolation on the precomputed grid. The total luminosity of each particle is computed as

$$L_{\rm CO} = \frac{X_{\rm H} m_{\rm g} l_{\rm CO}}{m_{\rm H}}, \quad (4)$$

where $X_{\rm H} = 0.76$ is the total hydrogen mass fraction (including all phases of hydrogen) and $m_{\rm g}$ is the gas particle mass. Gas with an ionized fraction greater than 10% is assigned $L_{\rm CO} = 0$, since our grid does not include the effects of photoionization.

To enable comparison with observations, we convert this luminosity to an inferred molecular hydrogen mass using

$$\frac{m_{\rm H_2,CO}}{M_\odot} = 2.3 \times 10^{-29} \frac{L_{\rm CO}}{\rm erg}\ {\rm s}^{-1}, \quad (5)$$

which incorporates both the mass-to-luminosity conversion factor $X_{\rm CO}$ from A. D. Bolatto et al. (2013) and the ^{12}CO $J = 1 \rightarrow 0$ line-luminosity conversion factor from P. Solomon & P. Vanden Bout (2005). Both values are fitted from solar neighborhood observations. This molecular mass can be further converted into the number of hydrogen molecules. In Figure 1 (upper right panel), we present the face-on synthetic $N_{\rm H_2,CO}$ column density map for the 720 Myr snapshot. The pixel size is chosen to be 1 pc, approximately twice the characteristic spatial resolution of our simulation, and this resolution is maintained for all synthetic observations in this work.

As is common practice in observational studies (e.g., S. E. Ragan et al. 2014; J. Abreu-Vicente et al. 2016), we adopt a constant $X_{\rm CO}$ conversion factor throughout the simulated galaxy. This approach helps to minimize discrepancies when comparing our synthetic GMF catalog with observational catalogs. However, there is strong theoretical and observational evidence that $X_{\rm CO}$ varies systematically with gas metallicity (e.g., S. C. O. Glover & M.-M. Mac Low 2011; R. Feldmann et al. 2012; A. D. Bolatto et al. 2013; M. Gong et al. 2020) and other physical properties such as temperature, velocity dispersion, and density structure (R. Shetty et al. 2011a, 2011b; D. Narayanan et al. 2011, 2012; L. Ramambason et al. 2024). Such environmental and structural dependencies introduce significant uncertainties into GMF mass measurements inferred from previous observational surveys. Due to current computational constraints, our simulations assume constant solar neighborhood values for the metallicity and ISRF strength rather than modeling their time-dependent evolution, an assumption that is consistent with the methodology of our synthetic observation algorithm. Consequently, the synthetic GMF catalog identified in Section 2.3 is considered reliable under these constant conditions but may not fully capture the influence of a varying galactic environment on the derived masses.

2.3. GMF Identification

The most common method used in previous observational studies to identify GMFs is to apply simple column density or integrated intensity thresholds to locate dense GMCs, followed by visual inspection to identify filamentary structures (S. E. Ragan et al. 2014; K. Wang et al. 2015; C. Zucker et al. 2015, 2018; J. Abreu-Vicente et al. 2016). Due to the large area of our simulated galaxy, we employ automated algorithms rather than visual inspection to search for filaments. Algorithms used in prior studies include DISPERSE (T. Sousbie et al. 2011), SCIMES (D. Colombo et al. 2015), FILFINDER (E. W. Koch & E. W. Rosolowsky 2015), and a customized minimum spanning tree (MST) algorithm (K. Wang et al. 2016; K. Wang & Y. Ge 2021). However, DISPERSE and SCIMES have been reported to have limited effectiveness in detecting elongated structures on large scales (C. Zucker et al. 2019), and MST requires a clump catalog as input. Therefore, we adopt FILFINDER to identify GMFs in our synthetic observations. FILFINDER can uniformly identify filamentary structures over a wide dynamic range of intensities and can measure filament properties such as lengths, widths, and radial profiles.

We apply FILFINDER in two different ways: one is to a face-on view of the galaxy, as shown in the upper right panel of Figure 1, and the other is to an edge-on view, as in real observations. These approaches are complementary in that the former lets us identify filaments more accurately and fast by eliminating line-of-sight (LOS) confusion,[4] while the latter is a truer representation of the process used to produce observed GMF catalogs.

The first step for the face-on case is to apply a mask to the face-on synthetic $N_{\rm H_2,CO}$ column density map shown in Figure 1. Previously adopted thresholds are typically 1σ–2σ above the mean background. For example, S. E. Ragan et al. (2014) use a ^{13}CO emission intensity threshold of $\sim$1 K km s^{-1}, while J. Abreu-Vicente et al. (2016) adopt a similar value, corresponding to $N({\rm H_2}) \simeq 0.87$–1.3×10^{21} cm^{-2}. The Herschel filaments identified by K. Wang et al. (2015) correspond to structures denser than $N({\rm H_2}) > 10^{21}$ cm^{-2}. To consistently identify filamentary structures across the simulated galaxy, we adopt a uniform threshold of $N_{\rm H_2,CO} = 1.0 \times 10^{21}$ cm^{-2}. In addition, we exclude the central region within a galactocentric radius of $R_{\rm gal} \leqslant 2.5$ kpc, as GMFs in previous observational catalogs are not located near the galactic center. FILFINDER is then used to reduce the isolated contours in the mask to single-pixel-wide skeletons representing filament spines. To remove spurious features caused by pixelization, we prune skeletons and branches shorter than 10 pc. These thresholds are motivated by two considerations: (1) the minimum GMF length observed in previous studies is $\sim$10 pc (see Figure 10 in C. Zucker et al. 2018); (2) structures smaller than 10 times our spatial resolution may not be fully resolved.

For each identified filament after pruning, we measure four key physical properties: length l, width w, mass $M_{\rm CO}$, and aspect ratio ar. The filament length is defined as the length of the longest path along the skeleton (the filament spine). Filament width is determined using the RADFIL package (C. Zucker & H. H.-H. Chen 2018), which performs perpendicular cuts across the spine, measures the length of each cut from one side of the filament contour to the other, and then takes the median value as the filament width. Filament mass is calculated as the sum of molecular mass inferred from the synthetic CO emission within the filament contour. We adopt three criteria for a filament to be classified as a GMF: $l \geqslant 10$ pc, $ar \geqslant 5$, and $M_{\rm CO} \geqslant 10^3\, M_\odot$. The minimum aspect ratio follows P. André et al. (2014), while the minimum mass ensures that each GMF is resolved by at least $\sim$10 gas

[4] In principle, we could also attempt to identify filaments in the full three-dimensional galaxy simulation using the FILFINDER3D module, which would provide even more accurate "true" filaments. However, we found that applying this package to a simulation as large as ours was prohibitively computationally expensive.

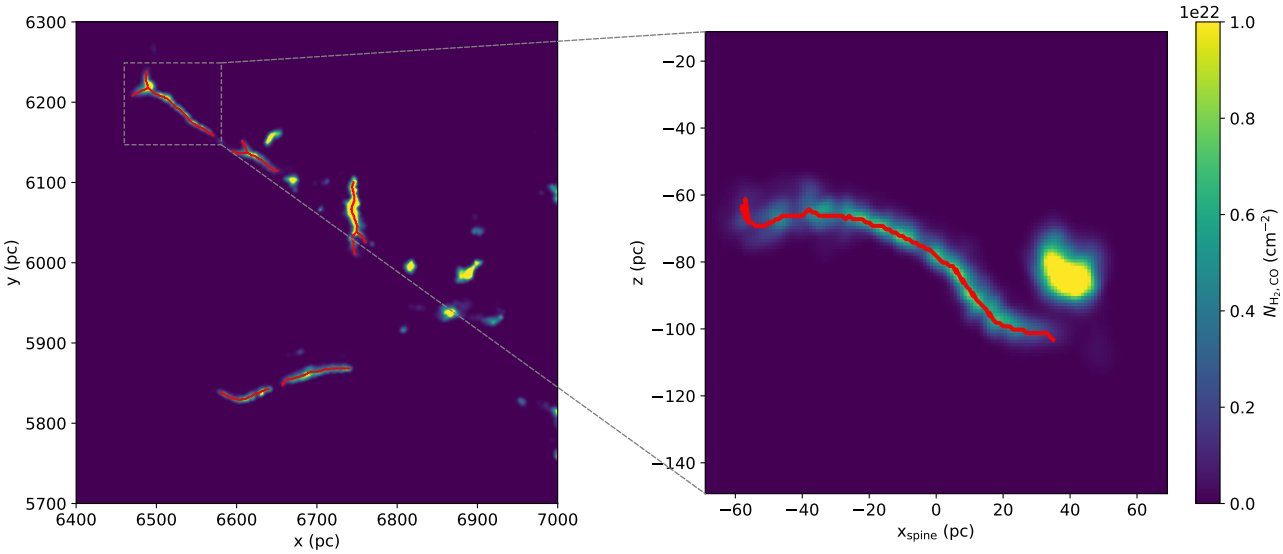

Figure 2. Left panel: face-on $N_{H_2,CO}$ column density map of a (600 pc)^2 region in the simulated galaxy. The spines of identified face-on GMFs are shown as red lines. Right panel: edge-on view of the selected GMF in the gray box in the left panel. Note that the connected filament in the edge-on view consists of two components in the face-on view.

particles. Applying these criteria yields 1042 GMFs in the face-on synthetic observation, forming our face-on synthetic GMF catalog. The spines of these GMFs are illustrated as red lines over a (600 pc)^2 region of the $N_{H_2,CO}$ column density map in the left panel of Figure 2.

To generate our in-plane (edge-on) views of these GMFs, each face-on GMF is projected along its minor axis, determined from the eigenvector corresponding to the smaller eigenvalue of the covariance matrix of the filament contour. The edge-on projection considers only gas particles within the face-on GMF contour to exclude foreground and background gas. We analyze the impact of projection effects on GMF physical property measurements in the Appendix. The projection is centered on the CO-traced molecular mass of the selected gas particles. For the edge-on column density map, the window size is the spine length plus 10 pc to avoid boundary effects, the north vector is aligned with the simulation z-axis (perpendicular to the galactic plane), and the resolution is 1 pc. The edge-on view of a selected GMF is shown in the right panel of Figure 2. GMFs in the edge-on maps are identified using the same procedure as for the face-on maps, yielding a catalog of 742 GMFs. The reduced number of GMFs arises because some face-on GMFs consist of multiple overlapping components that are merged along a single line of sight, and individual components may not satisfy the identification criteria in the edge-on view. Using synthetic observations from two perpendicular lines of sight ensures that our edge-on GMFs are spatially connected structures. We illustrate the spatial distribution of these GMFs in the simulated galaxy as the cyan contours in the upper right panel of Figure 1.

3. Results: Synthetic GMF Catalog

To assess whether the GMFs identified in our synthetic observations resemble those in previous catalogs, we compare four key physical properties of our edge-on synthetic GMF catalog to the observed values: length, width, mass, and linear mass. Length, width, and mass for each synthetic GMF were determined in Section 2.3, while linear mass is calculated as the ratio of GMF mass to length.

For observed Galactic GMFs, C. Zucker et al. (2018) classified them into four categories based on filament selection criteria and summarized their physical properties. The categories include the Milky Way Bone, GMF, large-scale Herschel, and MST Bone, abbreviated as "Bone," "GMF," "Herschel," and "MST." We present the distributions of length, width, mass, and linear mass as box-and-whisker plots in Figure 3. From the plot, we find that our synthetic GMFs closely reproduce the physical properties of the "GMF" category, which corresponds to the largest molecular structures observed in the Galaxy (S. E. Ragan et al. 2014; J. Abreu-Vicente et al. 2016). This agreement arises from two main factors: (1) filament widths in other categories are only around a few parsecs, which are close to the 1 pc spatial resolution of our synthetic observations; (2) the universal column density threshold we adopt is based on the observations of the "GMF" category. The effects of alternative filament identification algorithms are discussed in Section 5.1.

We also summarize additional physical properties of our synthetic edge-on GMFs in Table 1, including mean column density $\bar{N}_{H_2,CO}$, LOS velocity gradient $\Delta v_{LOS}/\Delta l$, velocity dispersion σ_v, and mean magnetic field strength B. The mean column density $\bar{N}_{H_2,CO}$ is obtained from the total molecular mass traced by CO emission within the filament mask divided by the mask area. The LOS velocity gradient is calculated as the ratio of the maximum v_{LOS} difference among all pixels inside the filament mask to the filament spine length l. Filament velocity dispersion[5] is computed as

$$\sigma_v = \sqrt{\sigma_{v,x}^2 + \sigma_{v,y}^2 + \sigma_{v,z}^2}, \tag{6}$$

where $\sigma_{v,i}$ ($i \in \{x, y, z\}$) is the CO-emission-weighted velocity dispersion of all gas particles within the filament mask along the i-axis. For the magnetic field, we first determine the

[5] Note that the velocity dispersion here is the intrinsic dispersion derived from 3D velocity vectors. The result indicates the upper limit of observed velocity dispersion, which is calculated from LOS 1D components.

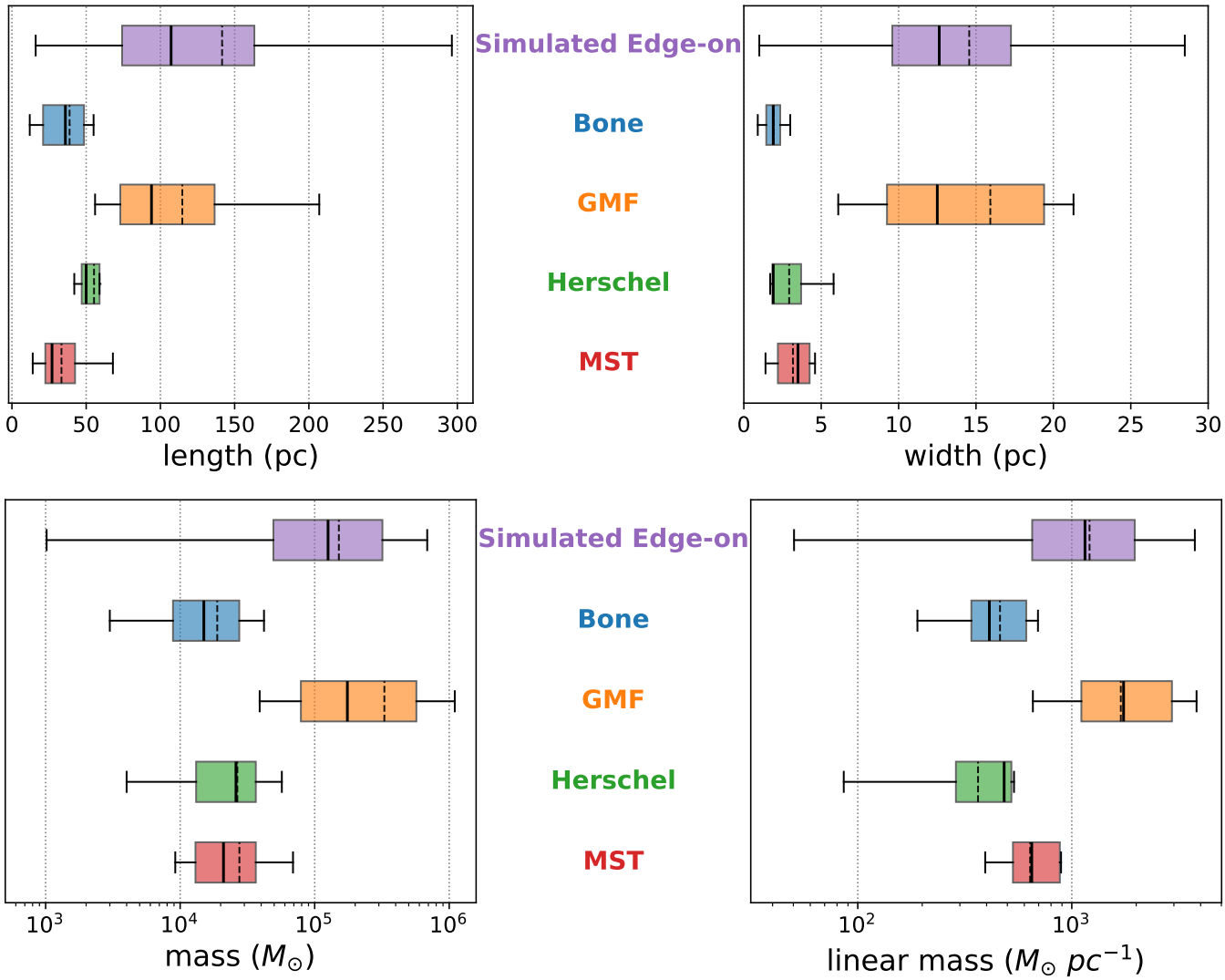

Figure 3. Box-and-whisker plots showing the distributions of GMF length (top left), width (top right), mass (bottom left), and linear mass (bottom right). Solid lines indicate the median, while dashed lines indicate the mean. Colors and labels in the center identify the data source of each GMF sample.

Table 1
Mean Values and Percentiles of Edge-on Synthetic GMF Properties

	$N_{H_2,CO}$ ($\times 10^{21}$ cm^{-2})	$\Delta v_{LOS}/\Delta l$ (km s^{-1} pc^{-1})	σ_v (km s^{-1})	B (μG)
Mean	5.75	0.048	5.31	15.88
25th percentile	3.81	0.028	3.05	10.85
50th percentile	5.10	0.040	4.48	14.58
75th percentile	6.89	0.055	6.50	19.13

magnitude of the field for all gas particles within the filament mask and then take the CO-emission-weighted mean. We do not perform a comparison to observations for these properties, as they are not available in all GMF catalogs.

The mean value of the synthetic $N_{H_2,CO}$ column density is similar to the typical value of 4.8×10^{21} cm^{-2} observed for the "GMF" category. The magnetic field strength (10–20 μG) is also consistent with values measured in GMCs (R. M. Crutcher 2012). Regarding the velocity dispersion, adopting the mean length $l \approx 140$ pc and mean width $w \approx 16$ pc of the edge-on GMFs gives a characteristic size $L = \sqrt{lw} \approx 47$ pc. Using Larson's law, σ_v (km s^{-1}) $= 1.10L$ (pc)$^{0.38}$ (R. B. Larson 1981), such a size corresponds to $\sigma_v \approx 4.8$ km s^{-1}, which lies between the median and mean velocity dispersions of our synthetic GMFs. LOS velocity gradients have not been systematically studied for ~100 pc long GMFs, but for comparison, A. A. Goodman et al. (2014) measured a gradient of 0.025 km s^{-1} pc^{-1} for the "Nessie" filament, comparable to the values found in our synthetic catalog. Therefore, our synthetic GMFs are consistent with real observations when considering these additional physical properties. K. Wang et al. (2016) and Y. Ge & K. Wang (2022) report median values of 0.33 km s^{-1} pc^{-1} and 0.47 km s^{-1} pc^{-1}, respectively, for the velocity gradients of their "MST" GMF catalogs, which are significantly larger than the result from our synthetic catalog. Such a discrepancy may originate from the velocity difference criteria applied in the MST algorithm, as explained in Section 5.1.

We also perform a one-dimensional (1D) virial analysis on the synthetic GMFs. As shown in Table 1, the velocity dispersions of the GMFs are much larger than the thermal velocity dispersion $c_s \sim 0.3$ km s^{-1} for $T \approx 20$ K, indicating that turbulent motions dominate their gravitational stability.

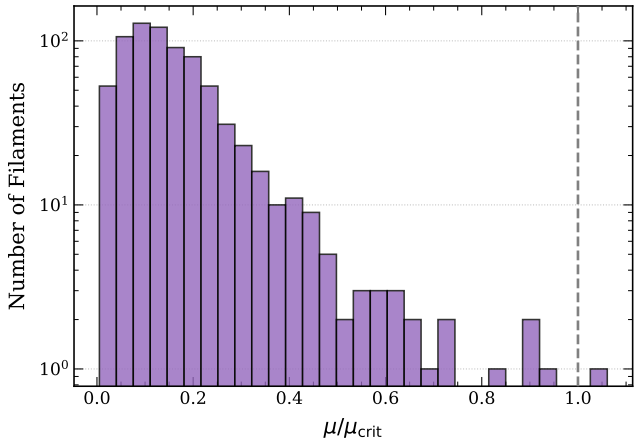

Figure 4. Histogram of the ratio between the synthetic GMF linear mass μ and the virial linear mass $\mu_{\rm vir}$. The vertical gray dashed line indicates $\mu/\mu_{\rm vir} = 1$.

The synthetic GMF virial line mass is computed as

$$\mu_{\rm vir} = \frac{2\sigma_v^2}{G} \sim \left(\frac{\sigma_v}{1\ {\rm km\ s^{-1}}}\right)^2 M_\odot\ {\rm pc}^{-1}, \tag{7}$$

where G is the gravitational constant. In Figure 4, we show a histogram of the ratio between the GMF linear mass μ and the virial line mass $\mu_{\rm vir}$. The figure demonstrates that nearly all synthetic GMFs are gravitationally subcritical.

4. Results: GMF Life Cycle

After identifying the synthetic GMFs, we trace their evolution across different simulation snapshots. The typical life cycle of an isolated GMF can be divided into three stages. The first is the *formation stage*, during which GMFs assemble from the accretion of atomic gas. The second is the *fragmentation stage*, when turbulent perturbations cause the GMFs to break into dense clumps, triggering rapid star formation. The third is the *dispersion stage*, where stellar feedback—primarily from massive stars—disperses the molecular gas. Owing to their large spatial extent, GMFs are influenced by physical processes acting across multiple scales. We illustrate the evolution of an example GMF as an animation in Figure 5. In the following, we discuss the roles of the dominant mechanisms during each stage of the GMF life cycle.

4.1. Formation Mechanism

4.1.1. Dominant Mechanism: Magnetized Turbulence

As discussed in Section 5 of A. Hacar et al. (2022), turbulence, magnetic fields, stellar feedback, and galactic dynamics all contribute to filament formation. The one-dimensional analysis in Figure 4 indicates that turbulence dominates over gravity for most GMFs. However, to fully assess the relative importance of different physical mechanisms, a three-dimensional virial analysis is required, both for the GMFs themselves and for the surrounding atomic regions where gas accretion occurs. This requires identifying the 3D counterparts of the 2D GMFs seen in synthetic observations. For each GMF, we first construct a cubic box with a side length 20 pc larger than the GMF length and interpolate the gas properties of all particles onto a 1 pc voxel grid. We then draw 3D molecular density contours centered on the GMF center of mass (CoM)

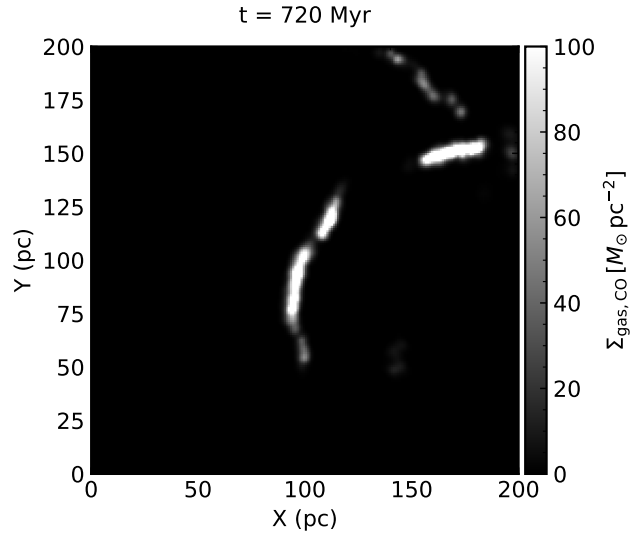

Figure 5. A static frame from the animated Figure 5. This animation, which runs for 14 s, shows the evolution of an example GMF over time. Each frame represents a face-on view of the surface density map from one snapshot. The simulation time of the corresponding snapshot is shown at the top.
(An animation of this figure is available in the online article.)

with thresholds $n_{\rm H_2,CO} \in \{0.5, 5, 25, 50, 75, 100\}\ {\rm cm^{-3}}$, where $n_{\rm H_2,CO}$ is the CO-derived molecular hydrogen number density. From these contours, we calculate the enclosed molecular mass $M_{\rm 3D}$ and compare it with the 2D mass estimate $M_{\rm 2D}$. The top panel of Figure 6 shows the median and interquartile range of $M_{\rm 3D}/M_{\rm 2D}$ as a function of threshold. We find that $M_{\rm 3D}/M_{\rm 2D} \sim 1$ at $n_{\rm H_2,CO} = 20\ {\rm cm^{-3}}$. We therefore adopt $n_{\rm H_2,CO} = 20\ {\rm cm^{-3}}$ as the fiducial threshold for identifying GMFs in 3D, as it ensures the consistency between the masses measured from 2D projections and 3D structures.

Although this threshold is much lower than both the mean density of the synthetic GMFs and the typical density of CO-bright gas ($\bar{n}_{\rm H_2,CO} \approx 100\ {\rm cm^{-3}}$ (A. D. Bolatto et al. 2013), it corresponds to the diffuse molecular-gas regime ($\sim$30 cm^{-3}) observed in the Milky Way (R. S. Klessen & S. C. O. Glover 2016). Moreover, this density is approximately where the molecular gas begins to transition from the CO-dark to the CO-bright phase in our synthetic observations. To illustrate this, we vary the $n_{\rm H_2,CO}$ threshold from 1 to 100 cm^{-3}, compute the ratio between the molecular hydrogen mass above each threshold and the total molecular hydrogen mass, and plot these ratios in the bottom panel of Figure 6. At the adopted threshold of $n_{\rm H_2,CO} = 20\ {\rm cm^{-3}}$, approximately 65% of the molecular mass is recovered, which is broadly consistent with the observed range (50%–67%) in the solar neighborhood (I. A. Grenier et al. 2005). Varying the threshold by a factor of 2 around 20 cm^{-3} changes the total mass of the identified 3D GMFs by only $\sim$10%, demonstrating the robustness of our subsequent analysis.

After linking 2D and 3D GMFs, we compute their gravitational potential energy E_g, magnetic energy E_B, and turbulent energy E_k, using the 3D voxel grid. The gravitational potential ϕ is obtained with the adaptive PYTREEGRAV library (M. Grudić & A. Gurvich 2021), yielding $E_g = \frac{1}{2}\sum \rho_i \phi_i$. The magnetic energy is given by $E_B = \frac{1}{8\pi}\sum B_i^2 V_i$, where $V_i = 1\ {\rm pc}^3$ is the voxel volume. The turbulent energy E_k is determined from the velocity dispersion relative to the mass-weighted mean

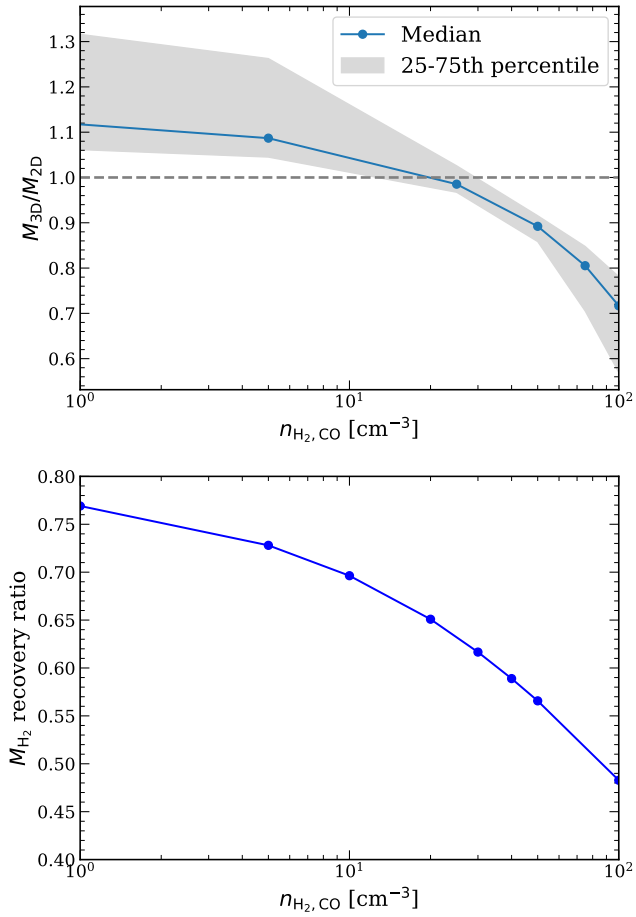

Figure 6. Top panel: ratio between the molecular mass from 3D contours surrounding the CoM of GMF M_{3D} and the molecular mass from 2D synthetic observations M_{2D}. The x-axis shows the value of the number density threshold of different 3D contours. The blue dotted line shows the median value of the ratios from the synthetic edge-on GMF catalog, while the gray band illustrates the 25th to 75th range of the ratios. Bottom panel: ratio between the molecular hydrogen mass above a given $n_{H_2,CO}$ threshold and the total molecular hydrogen mass.

velocity: $E_k = \frac{1}{2}\sum \rho_i[(v_{x,i} - \bar{v}_x)^2 + (v_{y,i} - \bar{v}_y)^2 + (v_{z,i} - \bar{v}_z)^2]$. These energies are calculated both within the GMF masks ($n_{H_2,CO} > 20$ cm^{-3}) and including the surrounding atomic regions ($n_H > 1$ cm^{-3}). The histograms in the left and middle panels of Figure 7 show the probability distribution functions (PDFs) of $(2E_k + E_B)/|E_g|$ and E_k/E_B. We find $(2E_k + E_B)/|E_g| \gg 1$ on both scales, indicating that magnetized turbulence dominates over gravity during mass accretion. Meanwhile, $E_k/E_B \sim 1$ suggests comparable contributions from turbulence and magnetic fields.

4.1.2. Role of Magnetic Field

In order to study the relative importance of the magnetic field across different density regimes, we calculate E_k/E_B and $|E_g|/E_B$ in 3D contours with four density levels: $n_H > 1$ cm^{-3}, $n_{H_2} > 5$ cm^{-3}, $n_{H_2} > 20$ cm^{-3}, and $n_{H_2} > 50$ cm^{-3}. Then we plot the 25th, 50th, and 75th percentiles of these energy ratios in the right panel of Figure 7. The results show that in the atomic regime ($n_H > 1$ cm^{-3}), the magnetic energy is comparable to the kinetic energy and dominant over gravitational energy, but becomes less important than the other two energy sources when molecules start to form.

To further evaluate the role of magnetic fields in GMF evolution, we examine their alignment with gas structures. We illustrate the mass-weighted B-field mean strength projection map surrounding an example GMF from two perspectives: a face-on view (panel (a)) and an edge-on view (panel (b)) in Figure 8. Observational studies of 2D projected fields typically employ the histogram of relative orientations, the alignment measure parameter, or the projected Rayleigh statistic (J. D. Soler et al. 2013; D. F. González-Casanova & A. Lazarian 2017; K. H. Yuen & A. Lazarian 2017; D. L. Jow et al. 2018) for this purpose, but since we have access to the full 3D structure in our simulations we opt to measure the degree of alignment between a pair of vector fields $\boldsymbol{v}_1$ and $\boldsymbol{v}_2$ directly by computing the distribution of the absolute value of cosine of the angle between them, $\mu_{\boldsymbol{v}_1,\boldsymbol{v}_2} = |\boldsymbol{v}_1 \cdot \boldsymbol{v}_2|/v_1 v_2$, where $v_1 = |\boldsymbol{v}_1|$ and similarly for v_2. If the two vector fields are randomly oriented, the PDF of μ is expected to be uniform between 0 and 1. In contrast, a median value of the PDF close to 0 indicates a preference for perpendicular orientations, while a value close to 1 indicates a preference for parallel orientations.

To justify our choice of 3D over 2D analysis, we quantify the magnetic field-to-spine alignment, $\mu_{\mathbf{B},\mathbf{spine}}$, for the example GMF in Figure 8. We compute this metric from three perspectives: face-on, edge-on, and in 3D space. The spines for the projected views are identified using FILFINDER (as in Section 2.3), while the 3D spine is derived from the mask in Section 4.1.1 using FILFINDERPPP, the 3D extension of FILFINDER. To account for variations along the filament, we divided each spine into 5 pc long segments. For each segment, we calculated the mean spine direction from its endpoints and the mean magnetic field direction from the average of B-field vectors within a 5 pc radius. We then computed $\mu_{\mathbf{B},\mathbf{spine}}$ for all segments in the three cases.

The resulting PDFs and median values are shown in panel (c) of Figure 8. The face-on view indicates a nearly parallel alignment, whereas the edge-on view shows a mix of parallel and perpendicular alignments. In contrast, the 3D analysis reveals no preferred alignment. These results demonstrate that projection effects can introduce significant uncertainties in alignment analysis, underscoring the necessity of 3D information for accurately determining the role of magnetic fields.

To directly study the role of the magnetic field in the dynamics of GMF, we first compute the distribution of cosine for the magnetic field and the density gradient, $\mu_{\boldsymbol{B},\nabla n_H}$, over all voxels, both inside GMFs ($n_{H_2,CO} \geqslant 20$ cm^{-3}) and in the surrounding atomic outskirts ($n_{H_2,CO} < 20$ cm^{-3}, $n_H > 1$ cm^{-3}). We plot the results in the left panel of Figure 9. The distributions show a very weak preference for perpendicular alignment in both regimes. We also compute the distribution of cosine angles between the magnetic field and relative gas velocity vectors, $\mu_{\boldsymbol{B},\boldsymbol{v}}$, which we show in the right panel of Figure 9. Here, we define the relative gas velocity of each voxel as the velocity at that position minus the mass-weighted mean velocity of the GMF. We find no significant evidence for a preferred alignment in either the GMFs or their atomic outskirts.

These results suggest that magnetic fields do not strongly regulate gas flow directions, particularly in the accreting envelopes of GMFs. Instead, similar to turbulence, their main role during GMF formation is to provide support against gravity rather than to channel gas inflows.

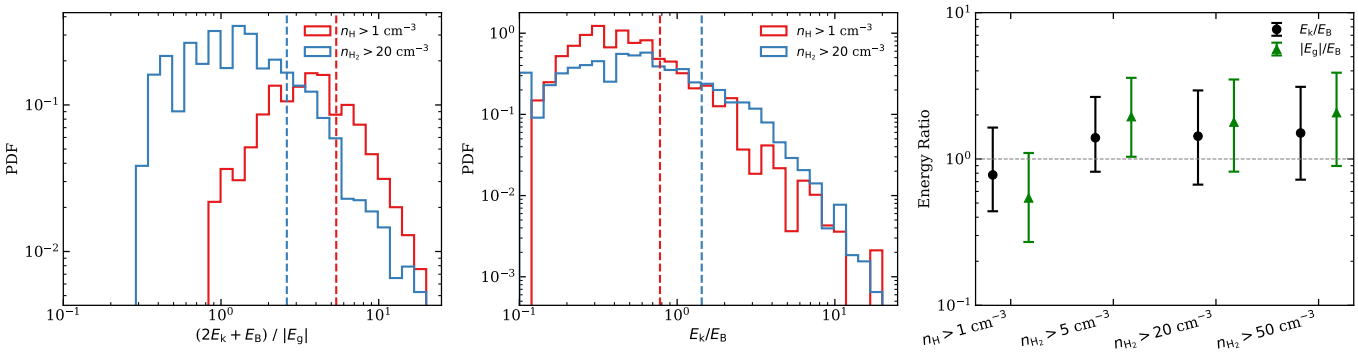

Figure 7. Left panel: PDFs of $(2E_k + E_B)/|E_g|$. The red histogram shows the PDF from 3D number density contours, corresponding to the atomic gas region containing GMF. The blue histogram shows the PDF from GMF itself. The vertical lines represent the median values of the histograms with the same color. Middle panel: same as the left panel, but showing the PDFs of E_k/E_B. Right panel: median energy ratios vs. density threshold. Black circles and green triangles represent E_k/E_B and $|E_g|/E_B$, respectively, with error bars showing the interquartile range (25th–75th percentiles).

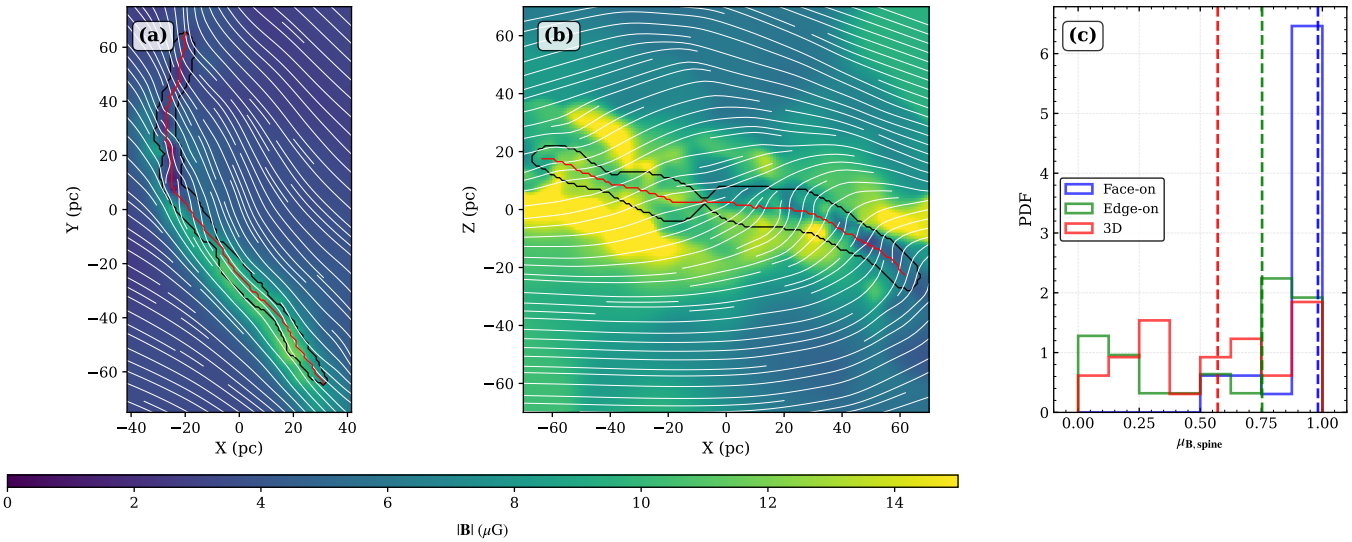

Figure 8. (a) Face-on view of the magnetic field strength $|\boldsymbol{B}|$ surrounding an example GMF with magnetic field streamlines (white lines) overlaid. The filament spine is indicated by the red line, and the GMF boundary is outlined in black. (b) Same as (a), but showing the edge-on view projected along the GMF's minor axis. (c) PDFs of the cosine of the angle between the magnetic field vector and the filament spine, $\mu_{\mathbf{B},\mathbf{spine}}$, for face-on view (blue), edge-on view (green), and 3D space (red). The vertical dashed lines indicate the median values for each distribution.

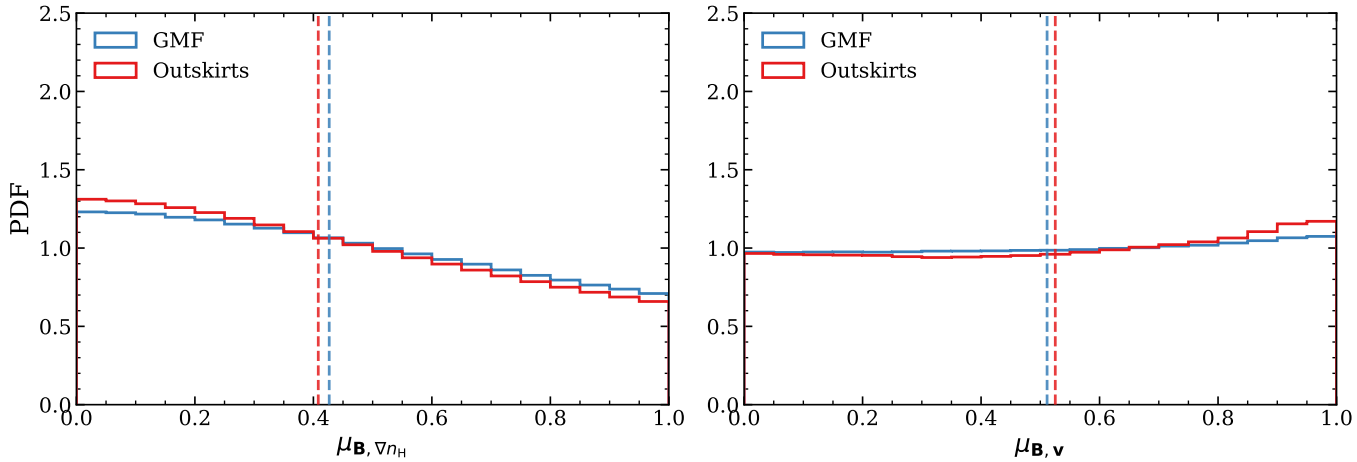

Figure 9. Distribution of cosine angles between magnetic field vectors and (left) density gradients ∇n_H and (right) relative velocity vectors $\boldsymbol{v}$. Blue and red histograms represent GMFs ($n_{H_2} > 20$ cm^{-3}) and atomic outskirts ($n_{H_2} < 20$ cm^{-3}, $n_H > 1$ cm^{-3}), respectively. Dashed vertical lines indicate median values.

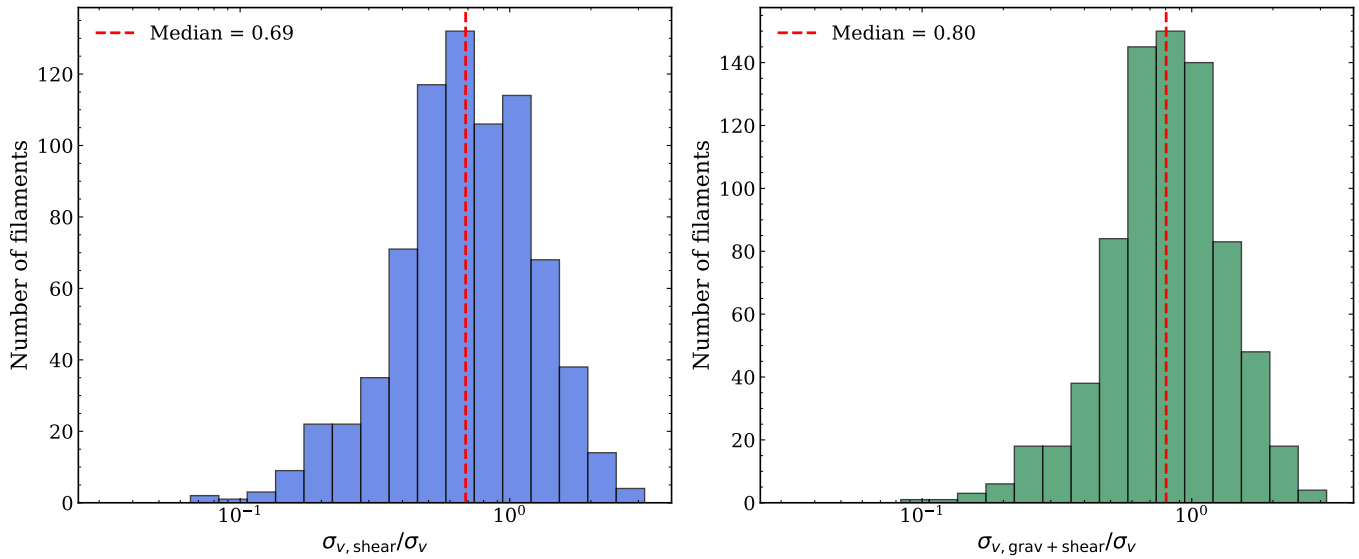

Figure 10. Left: histogram of the ratios between shear-induced velocity dispersion and total velocity dispersion. Right: same as left, but including contributions from both shear and self-gravity. The red dashed line marks the median ratio.

4.1.3. Source of Turbulent Energy

Since magnetized turbulence is the main driving mechanism during the GMF formation phase, we now examine the physical processes that inject such turbulent energy. Possible contributors include gravitational instabilities, galactic rotation, and stellar feedback (B. G. Elmegreen & J. Scalo 2004). Given the large spatial scale of the simulated GMFs (∼100 pc), galactic shear is expected to dominate.

To quantify this, we first derive the angular velocity profile $\Omega(r)$ by averaging over radial bins of 50 pc. For each edge-on GMF, we measure its projected radial extent l_r, and following Y.-H. Xie & G.-X. Li (2025), define the shear-induced velocity dispersion as

$$\sigma_{v,\mathrm{shear}} = \kappa l_r = r l_r \left| \frac{d\Omega(r)}{dr} \right|, \tag{8}$$

where κ is the local shear rate and r is the galactocentric radius of the GMF's center of mass. The histogram of $(\sigma_{v,\mathrm{shear}}/\sigma_v)$ in the left panel of Figure 10 shows that shear typically accounts for ∼70% of the total velocity dispersion.

We next consider the contribution from self-gravity. As shown in Figures 4 and 7, most GMFs are subcritical and therefore not undergoing global collapse. Instead, we estimate an upper limit to the gravitational contribution, defined as the dispersion required to maintain linear virial equilibrium:

$$\sigma_{v,\mathrm{grav}} = \left(\frac{GM}{2l}\right)^{1/2}. \tag{9}$$

Combining both contributions gives

$$\sigma_{v,\mathrm{grav+shear}} = (\sigma_{v,\mathrm{grav}}^2 + \sigma_{v,\mathrm{shear}}^2)^{1/2}. \tag{10}$$

As shown in the right panel of Figure 10, the median ratio $(\sigma_{v,\mathrm{grav+shear}}/\sigma_v)$ is ∼80%, only ∼10% higher than the shear-only case. Thus, self-gravity plays a much smaller role in driving turbulence than galactic shear.

4.1.4. Role of Stellar Feedback

The remaining ∼20% of the turbulent energy likely originates from stellar feedback, which can strongly reshape the gas distribution and promote filamentary structures due to its anisotropic nature. Directly quantifying this effect is difficult because feedback interacts nonlocally with the galactic environment. Instead, we test its impact statistically by correlating the number of GMFs with feedback strength in the surrounding ISM.

We divide the face-on galactic map (Figure 1) into square patches of side length 2.5 kpc, large enough to capture the local environment while yielding more than 30 regions for systematic comparison. For each patch, we compute (1) the total gas mass, (2) the number of GMFs with centers inside the patch, (3) the number of recent (1–10 Myr) SNe, and (4) the total Hα luminosity $L_{\mathrm{H}\alpha}$ tracing photoionization. To minimize the bias from uneven mass distribution, we normalize GMF counts, SNe, and $L_{\mathrm{H}\alpha}$ by the gas mass in each patch.

The correlations are shown in Figure 11. We find that the number of GMFs increases with both the local SNe rate and Hα luminosity. The Spearman coefficients are $R_s = 0.64$ for GMF number versus SNe and $R_s = 0.66$ for GMF number versus $L_{\mathrm{H}\alpha}$, both indicating significant positive monotonic trends. These results suggest that stellar feedback from massive stars enhances the formation of GMFs. However, we cannot from this analysis alone rule out the possibility that the causation runs in the other direction—that the presence of filaments causes (or shares a common cause with) star formation, which in turn leads to stronger feedback in locations where filaments are found. Additional simulations without stellar feedback physics are still needed to directly evaluate the role of stellar feedback in GMF formation.

4.2. GMF Evolution

When tracing the evolution of simulated GMFs, a common pathway is fragmentation into a number of dense clumps. Figure 12 illustrates this process for one example GMF: at $t = 720$ Myr (top panel), the structure appears as a long, coherent filament, while by $t = 730$ Myr (bottom panel), it has

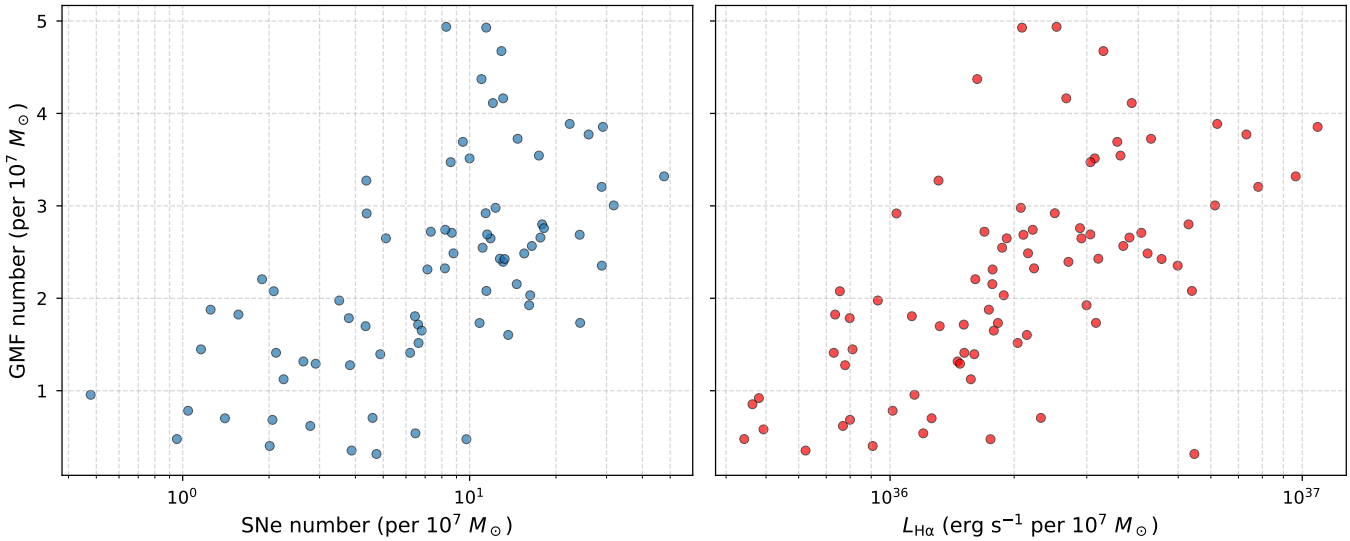

Figure 11. Number of GMFs per unit gas mass in (2.5 kpc)^2 patches, plotted against the number of recent SNe (left) and the total Hα luminosity $L_{H\alpha}$ (right). All variables are normalized by patch gas mass.

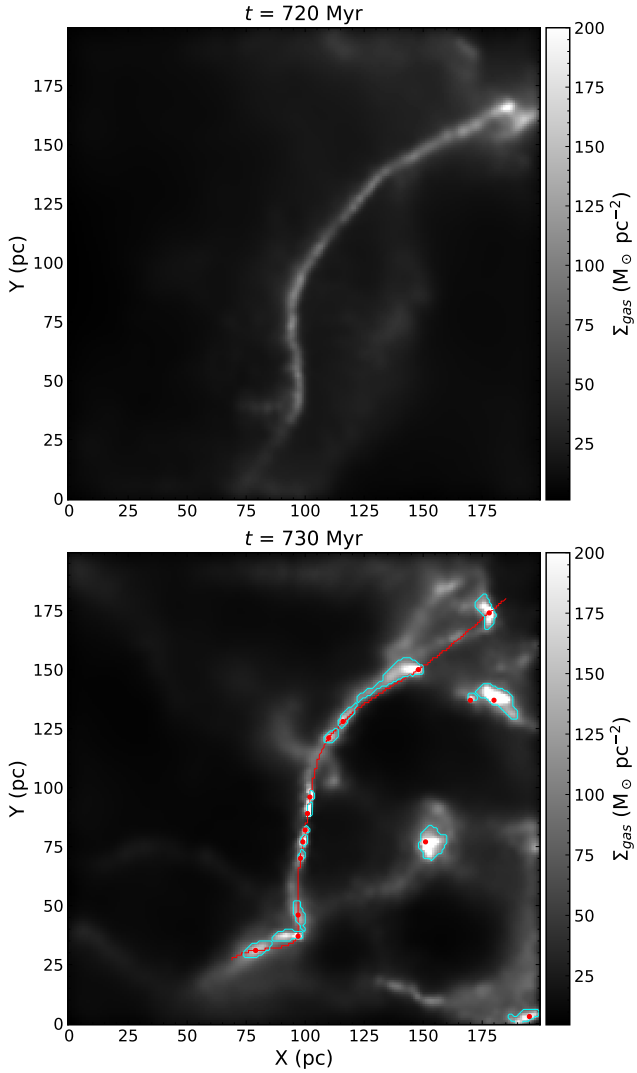

Figure 12. Gas surface density maps of a representative GMF at $t = 720$ Myr (top) and $t = 730$ Myr (bottom). In the later stage, cyan contours mark clumps identified using ASTRODENDRO; red dots indicate the local maxima of clumps; and red lines connect clumps with similar 3D velocities (differences <5 km s^{-1}).

fragmented into a dozen compact clumps distributed along the original filament spine.

Two classical theoretical frameworks have been widely invoked to explain such fragmentation. The first is the spherical Jeans instability model (J. H. Jeans 1902), which predicts local gravitational collapse if perturbations exceed the Jeans length,

$$l_{\rm J} = c_{\rm s}\sqrt{\frac{\pi}{G\bar{\rho}}} = \sqrt{\frac{\pi k_{\rm B} T}{\mu m_{\rm p} G\bar{\rho}}}, \tag{11}$$

where $\mu = 2.33$ is the mean molecular weight of molecular gas and $m_{\rm p}$ is the proton mass. In this scenario, the mean clump separation after fragmentation is expected to be comparable to $l_{\rm J}$.

A second framework is the "sausage" instability model, which considers the fragmentation of a self-gravitating fluid cylinder (S. Chandrasekhar & E. Fermi 1953; M. Nagasawa 1987). In this case, the average spacing between clumps is set by the critical wavelength of the fastest-growing unstable mode. For an isothermal infinite gas cylinder with scale height H, the critical wavelength is

$$\lambda_{\rm crit} = 22H, \tag{12}$$

where

$$H = \sqrt{\frac{c_{\rm eff}^2}{4\pi G\rho_{\rm c}}}, \tag{13}$$

$c_{\rm eff}$ is the effective sound speed and $\rho_{\rm c}$ is the central gas density of the filament (M. Nagasawa 1987; S.-I. Inutsuka & S. M. Miyama 1992).

While useful for providing insight, this simplified model neglects magnetic fields and self-rotation of the filament. To incorporate these effects, F. Nakamura et al. (1993) and T. Hanawa et al. (1993) derived a more general expression, showing that the characteristic spacing is related to the filament structure itself:

$$\lambda_{\rm crit} = 5.14\ {\rm FWHM}, \tag{14}$$

where FWHM is the full width at half-maximum of the GMF column density profile.

In order to examine which theoretical model best describes the fragmentation process of the simulated GMFs, we trace the evolution of selected GMFs to the fragmentation stage, determine the average spacings between clumps, and compare the values to those predicted by theoretical models. Such analysis is a multi-step process that combines spatial clustering, curve fitting, and spectral analysis. The first step is to select GMFs with $ar > 10$ and no significant branches (branch lengths larger than 10 pc). The reason is that clumps formed on a single-branch, very elongated structure make it easier for later average spacing calculation and model testing. After selection, we have 35 GMFs remaining. The second step is to trace the evolution of each GMF by plotting square gas surface density $\Sigma_{\rm gas}$ maps for each snapshot since $t = 720$ Myr. Each map is centered on the CoM of the GMF with a side length 20 pc longer than the GMF length and a pixel size of 1 pc. We choose true $\Sigma_{\rm gas}$ maps over synthetic CO observations to more precisely capture the underlying physical mechanisms. Then we use ASTRODENDRO (T. Robitaille et al. 2019) to find dense clumps from the $\Sigma_{\rm gas}$ maps. Our GMF identification threshold $N_{\rm H_2,CO} = 1.0 \times 10^{21}\,{\rm cm}^{-2}$ corresponds to a gas surface density $\Sigma_{\rm gas,min} = 20\,M_\odot\,{\rm pc}^{-2}$ with a hydrogen mass ratio of 0.76. Therefore, for consistent comparison across GMFs, when computing the dendrogram, we set the *min_value* (clump threshold) to $5\Sigma_{\rm gas,min} = 100\,M_\odot\,{\rm pc}^{-2}$, *min_delta* (clump minimum height) to $\Sigma_{\rm gas,min}$, and *min_npix* (clump minimum size) to 5 pixels. We find that 21 GMFs out of the 35 selected ones fragment into at least three clumps during the evolution tracing. Other GMFs stop fragmenting mainly due to environmental disturbances, such as CCC. These 21 GMFs form our subsample for theoretical model testing.

For each GMF in the subsample, we choose the snapshot with the most identified clumps, then group the clumps by velocity similarity using hierarchical clustering with a maximum 3D velocity difference of $5\,{\rm km\,s}^{-1}$. The most populous velocity group is selected, and its constituent clumps are connected via an MST algorithm to establish their spatial ordering along the filament's principal axis. A cubic spline is then fitted through the ordered clump positions, extended by 10 pc at both ends to capture the full filament extent. We plot the identified clumps and the spline fitted from the example GMF as cyan contours and the red line in the bottom panel of Figure 12, respectively. The surface density is extracted along this spline curve and smoothed using a Gaussian kernel with a 3 pc standard deviation to reduce noise. Finally, the Lomb–Scargle periodogram analysis is applied to the smoothed density profile, with a maximum period of half the curve length and a minimum period of the smoothing kernel size. The dominant period is identified as the wavelength corresponding to the peak power in the resulting power spectrum, with statistical significance assessed using a 75% false alarm probability threshold.

The smoothed density profile and the fitted oscillation period of the example GMF are shown in Figure 13. From the plot, we can see that there exist two main oscillation modes with spatial periods of ≈20 and 40 pc. The reason for multiple modes is that the galactic environment is not exactly the same along the GMF. We take the period with the maximum power as the observed oscillation period $\lambda_{\rm obs}$. For each GMF in the subsample, we first determine its Jeans length using the mean temperature and mean gas density in the 3D mask surrounding its CoM ($n_{\rm H_2,CO} \geqslant 20\,{\rm cm}^{-3}$). We then fit the FWHM of the GMF column density distribution from the $\Sigma_{\rm gas}$ map with the RADFIL package (C. Zucker & H. H.-H. Chen 2018), and calculate $\lambda_{\rm crit}$. We plot the histograms of ratios between theoretical period predictions and $\lambda_{\rm obs}$ in Figure 14. From the plot, we find that $l_{\rm J} \sim 0.5\lambda_{\rm obs}$, and $\lambda_{\rm crit} \sim 0.9\lambda_{\rm obs}$. Therefore, in the selected GMFs, the sausage instability model almost perfectly predicts the fragmentation period. The fragmentation process of the GMF is controlled by perturbations from MHD turbulence, rather than self-gravity.

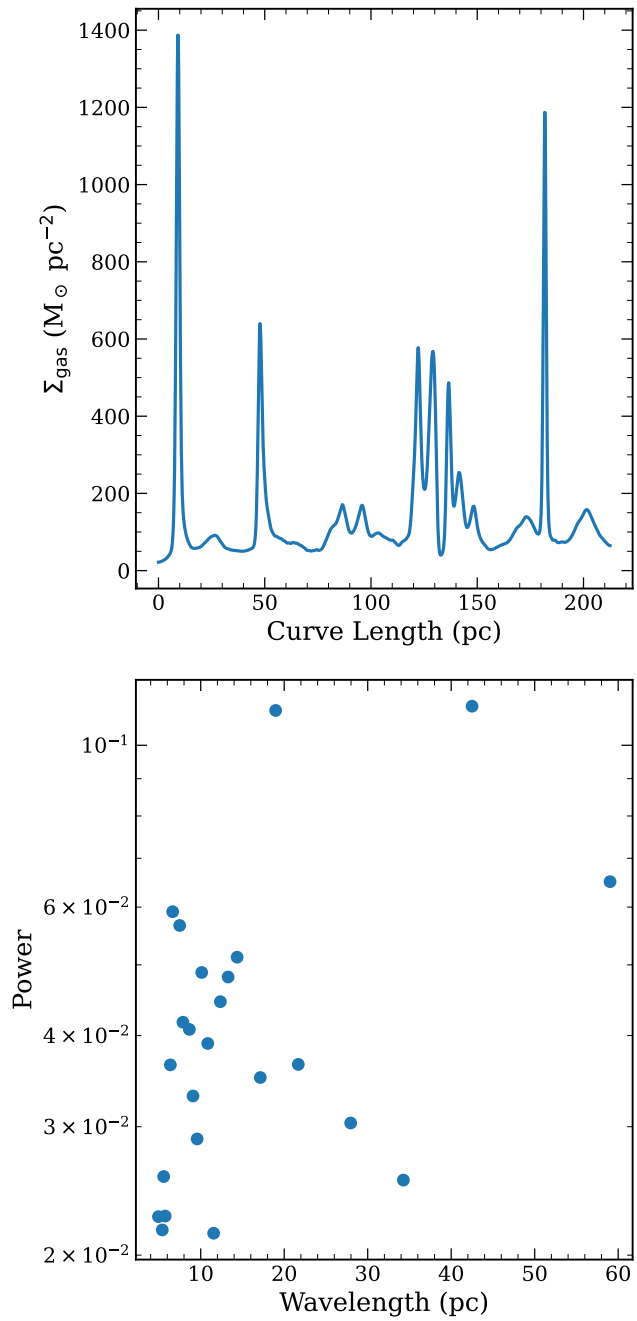

Figure 13. Fragmentation period analysis of the example GMF at $t = 730$ Myr. Top panel: smoothed $\Sigma_{\rm gas}$ profile along the curve connecting clumps with similar velocity. Bottom panel: power spectrum from Lomb–Scargle periodogram analysis of the $\Sigma_{\rm gas}$ profile, with statistically significant peaks (confidence level ⩾ 75%) marked as blue dots.

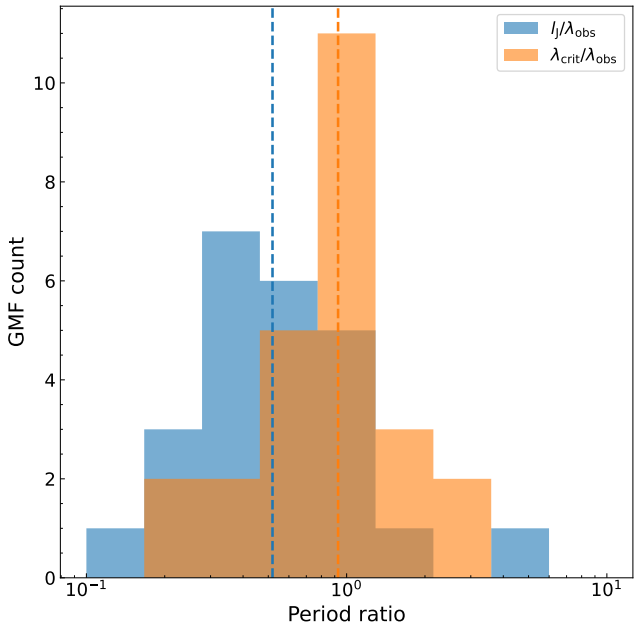

Figure 14. Comparison of theoretical fragmentation periods with observed clump spacing in selected GMFs. The histograms show the distribution of period ratios for two theoretical models: l_J/λ_{obs} (blue) and $\lambda_{crit}/\lambda_{obs}$ (orange). The dashed vertical lines indicate the median values for the distribution with the corresponding color.

Such fragmentation processes create clumps dense enough for local gravitational collapse. By tracing the evolution of the GMFs selected above, we find that for all stars formed inside these GMFs, only 18% on average form before the snapshot where most clumps are identified, indicating that fragmentation acts as the trigger of star formation inside GMFs. Therefore, magnetic turbulence plays two main roles in GMF evolution: it supports GMFs against global gravitational collapse, while its perturbations enable local star formation.

However, not all GMFs undergo the fragmentation process, as in the example shown in Figure 12, since CCCs are another common scenario in GMF evolution. Such collisions can complicate the morphology of GMFs and interrupt ongoing fragmentation. By tracing the GMCs with $M_{CO} > 10^3\,M_\odot$ from snapshot $t = 720$ to 730 Myr, we find that 55.5% of them merge with other GMCs during this period. For our GMFs, this fraction increases to 72.6% because of their larger sizes. We conclude that most GMFs experience CCC during their evolution, while the remaining isolated GMFs fragment into dense clumps as predicted by the sausage instability model.

4.3. GMF Destruction

For an isolated molecular cloud, stellar feedback from stars formed within the cloud can destroy its molecular mass, and its lifetime can be easily quantified by measuring the ratio of molecular mass over time. However, as our GMFs evolve in a realistic galactic environment, they experience high rates of CCC. Such collisions can not only disrupt the filamentary structure of a GMF but also prolong its existence as a GMC due to mass accretion, making it harder to quantify its lifetime. Here, we provide two timescales to describe the GMF life cycle: the first, t_{fil}, is the timescale over which a GMF remains filamentary before dispersion, fragmentation, or CCC; the second, t_{H_2}, is the half-life of gas particles in the identified GMFs remaining molecular.

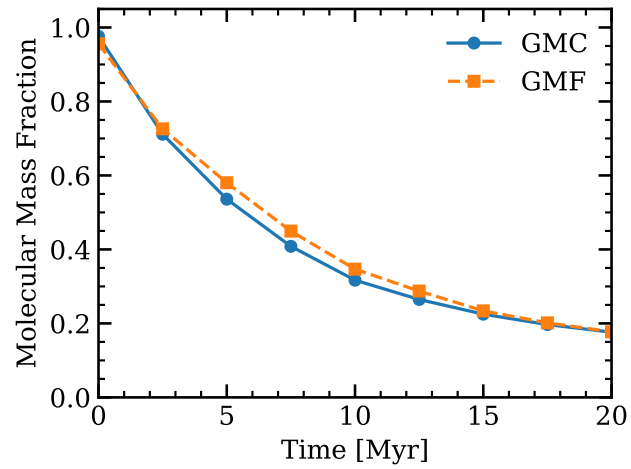

Figure 15. Evolution of molecular mass fraction over time for nonfilamentary GMCs (blue) and GMFs (orange).

To determine t_{fil}, we trace the face-on $\Sigma_{gas,CO}$ maps centered on the CoM of each synthetic GMF throughout our simulation snapshots, using map side lengths equal to the GMF length, and determine the total time over which at least one GMF can be identified from these maps using the same criteria as in Section 2.3. From the median of all results, we find $t_{fil} = 14^{+2}_{-5}$ Myr, where the uncertainties indicate the 25th and 75th percentiles. With further analysis on the evolution of GMF length and clump numbers, we find that during t_{fil}, it takes on average ~12 Myr for a GMF to grow to its maximum length since its formation, then takes ~2 Myr to fragment into the largest number of clumps.

As for t_{H_2}, we use DESPOTIC to compute the molecular mass fraction of all gas particles in the GMFs, defining gas particles with at least 50% molecular mass as being in the molecular phase. We trace these particles from the snapshot at which they are identified to the end of the simulation (20 Myr in total), and determine the molecular mass fraction at each snapshot. A similar analysis is performed for nonfilamentary GMCs ($ar < 5$) for comparison, as shown in Figure 15. We find no significant difference in the molecular mass destruction rate between GMCs and GMFs. From the plot, the molecular gas half-life is determined to be $t_{H_2} \approx 7$ Myr, roughly half of t_{fil}. We conclude that GMF destruction occurs on a timescale of 10–15 Myr, driven by turbulent shocks and stellar feedback in our simulation. Our finding that the chemical lifetime of H_2 is significantly smaller than the lifetime of the Eulerian molecular structures that those H_2 molecules comprise is consistent with the results of S. M. R. Jeffreson et al. (2024), who observe a similar phenomenon in simulations of a dwarf galaxy.

5. Discussion

5.1. GMF Identification Algorithm

As shown in Figure 3, the physical properties of our synthetic GMFs are close to the "GMF" catalog in real observations, and we have claimed that the reason for this similarity is primarily that we adopt a column density threshold for GMF identification similar to that used to produce the observed catalog. This raises an obvious question: if we adopt different identification algorithms, can we obtain objects with properties similar to those of other published

catalogs? This in turn will help answer the question of whether these catalogs are identifying distinct objects or whether they are just sampling different parts of the same structures.

To answer these questions, we start with the "Bone" and "Herschel" catalogs. These objects are identified by visual inspection, and thus lack a universal threshold, but since these structures tend to have smaller sizes and masses compared to those identified as GMFs, we increase the column density threshold in our identification algorithm to $N_{\rm H_2,CO} = 5.0 \times 10^{21}\,{\rm cm}^{-2}$ and $N_{\rm H_2,CO} = 1.0 \times 10^{22}\,{\rm cm}^{-2}$ to test whether structures identified by these thresholds are reasonable matches to observed catalogs. We show the physical properties of the synthetic structures identified with these two higher column density thresholds—along with the lower threshold of $1.0 \times 10^{22}\,{\rm cm}^{-2}$ we have adopted up to this point—as the top three box-and-whisker plots in Figure 16. We find that after applying the highest threshold ($N_{\rm H_2,CO} = 1.0 \times 10^{22}\,{\rm cm}^{-2}$), the identified structures match the "Bone" and "Herschel" catalogs in terms of their lengths, but their widths, masses, and linear masses remain significantly larger. Notably, the linear mass distribution remains nearly unchanged across the three thresholds, indicating that our synthetic structures are self-similar over an order of magnitude in column density. However, this may well be a limitation of our simulation resolution: the "Bone" and "Herschel" objects are typically $w \sim 1$–4 pc wide and have linear masses of $\mu \sim 300$–$500\,M_\odot\,{\rm pc}^{-2}$, implying typical densities $\rho \sim \mu/w^2 \sim 2$–20×10^{-21} g cm^{-3}; for our simulation mass resolution $m_{\rm res} = 90\ M_\odot$, the corresponding linear resolution is $(\rho/m_{\rm res})^{-1/3} \sim 0.6 - 1.7$ pc. Thus, the widths of objects like those found in the observed "Bone" and "Herschel" catalogs would be resolved by at most a handful of fluid elements in our simulation, suggesting that our failure to produce objects as thin as the "Bone" and "Herschel" catalogs may be nothing more than a resolution effect.

The "MST" catalog from K. Wang et al. (2016) is identified using a completely different method: instead of searching for continuous structures in column density maps, filaments are built by connecting adjacent, velocity-consistent dense clumps. To reproduce this catalog from our simulation, we first identify dense clumps from the face-on galactic $\Sigma_{\rm gas}$ map following the procedure in Section 4.2, and compute the molecular-mass-weighted 3D velocity for each clump. We then build MST trees representing GMFs following the methodology of K. Wang et al. (2016):

1. Each MST filament contains at least five clumps.
2. The separation between connected clumps is less than 10 pc.
3. The norm of the velocity difference between connected clumps is less than 2 km s^{-1}.
4. Linearity $f_L > 1.5$, defined as the ratio between the spread (standard deviation) along the MST's major axis and that along the minor axis.
5. Total filament length is at least 10 pc.

Using these criteria, we find 17 synthetic MST GMFs from the snapshot at $t = 720$ Myr. Their lengths are measured as the total MST tree length, widths as the mean major-axis lengths of the associated clumps, masses as the total clump masses, and linear masses as mass divided by length. The distributions of these properties are shown as the "Synthetic MST" box plots (gray) in Figure 16, and generally agree well with the observed MST catalog. The linear masses of the synthetic MSTs show a slightly broader range, which can be narrowed by increasing the clump identification $\Sigma_{\rm gas}$ threshold to reduce individual clump mass.

From this comparison, we confirm that our simulation can reproduce the MST catalog from observations. Only one of the 17 synthetic MSTs overlaps with the previously identified synthetic GMFs, consistent with the lack of overlap seen between observed catalogs (C. Zucker et al. 2018). This indicates that MSTs do not trace the high-$\Sigma_{\rm gas}$ regions inside continuous structures, but rather the GMFs in their later fragmentation stage. In future work, we plan to trace the evolution of synthetic MSTs backward to build theoretical models capable of recovering the initial conditions of GMFs from the observed clump properties.

5.2. GMF versus GMC

The galactic simulation results by A. Duarte-Cabral & C. L. Dobbs (2016) suggest that GMFs are an elongated, skinny, and massive subset of GMCs. However, this is largely a consequence of the adopted GMF identification criteria. To study whether GMFs have intrinsic differences from non-filamentary GMCs, we identify GMCs from synthetic face-on CO observations as contours with $N_{\rm H_2,CO} \leqslant 10^{21}\,{\rm cm}^{-2}$ and aspect ratio $ar < 5$. We then compare three physical properties for both GMFs and GMCs that can be reproduced in observations to test whether these objects are distinct in their density structures, SFRs, and dynamical timescales: the PDF of $N_{\rm H_2,CO}$, the star formation efficiency per freefall time $\epsilon_{\rm ff}$, and the crossing time $t_{\rm cross}$.

The $N_{\rm H_2,CO}$ PDF is determined from all pixels within the column density masks of all GMCs or GMFs, and plotted in the left panel of Figure 17 as blue for GMCs and red for GMFs. The PDF of GMFs is clearly shifted toward higher column densities, likely due to their larger masses or more compact geometries, but the overall shift is relatively small, $\approx$0.25 dex in the median.

The observed star formation efficiency per freefall time $\epsilon_{\rm ff}$ is calculated following the corrected form in Z. Hu et al. (2021):

$$\epsilon_{\rm ff} = \frac{t_{\rm ff}}{t_{\rm dep}} = \sqrt{\frac{3\pi}{32G\rho_g}}\,\frac{\dot{M}_*}{M_{\rm gas}}, \tag{15}$$

where $t_{\rm ff}$ is the freefall time, $t_{\rm dep}$ the gas depletion time, ρ_g the average gas volume density corrected by the Gini coefficient, $\dot{M}_*$ the SFR, and $M_{\rm gas}$ the total gas mass. For each GMC or GMF contour, we select stellar particles younger than 2 Myr (covering type I and II young stellar objects) and compute $\dot{M}_*$ as the total stellar mass divided by 2 Myr. The volume density $\rho_{\rm 2D}$ is determined from 2D contours assuming spherical GMCs and cylindrical GMFs. The Gini coefficient g of $\Sigma_{\rm gas}$ is determined from all pixels within the contour, then used to calculate ρ_g as

$$\rho_g = 10^{4.6g-0.93}\rho_{\rm 2D}. \tag{16}$$

The resulting PDFs of $\epsilon_{\rm ff}$ are shown in the middle panel of Figure 17. GMFs have a median $\epsilon_{\rm ff}$ that is $\sim$0.3 dex, or 2 times lower, than GMCs.

This difference likely reflects that in our synthetic observations, the objects identified as GMFs are dynamically young and have not yet fully fragmented into dense, star-forming

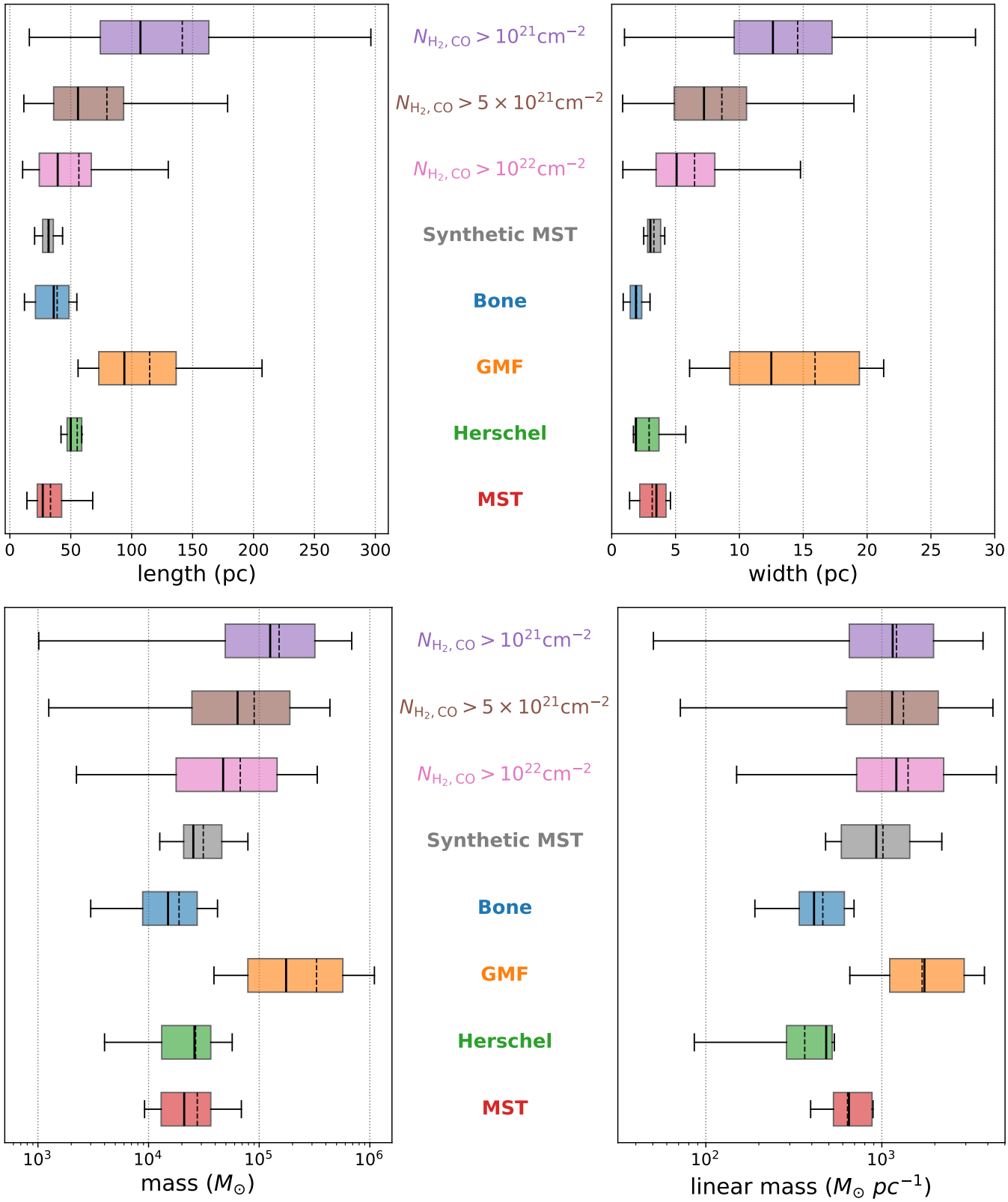

Figure 16. Same as Figure 3, but including box-and-whisker plots from synthetic GMFs identified with different N_{H_2} thresholds (top three rows) and synthetic GMFs identified with the MST algorithm (fourth row).

clumps. Because the observed value of ϵ_{ff} represents an integration over past star formation, a selection that picks out predominantly younger objects is likely to yield a systematically lower ϵ_{ff}. This is the converse of the more familiar effect whereby selections that pick out evolved regions where much of the gas has been dispersed—for example, catalogs of H II regions—yield artificially high ϵ_{ff} values (R. Feldmann & N. Y. Gnedin 2011; M. R. Krumholz et al. 2019). Both trends

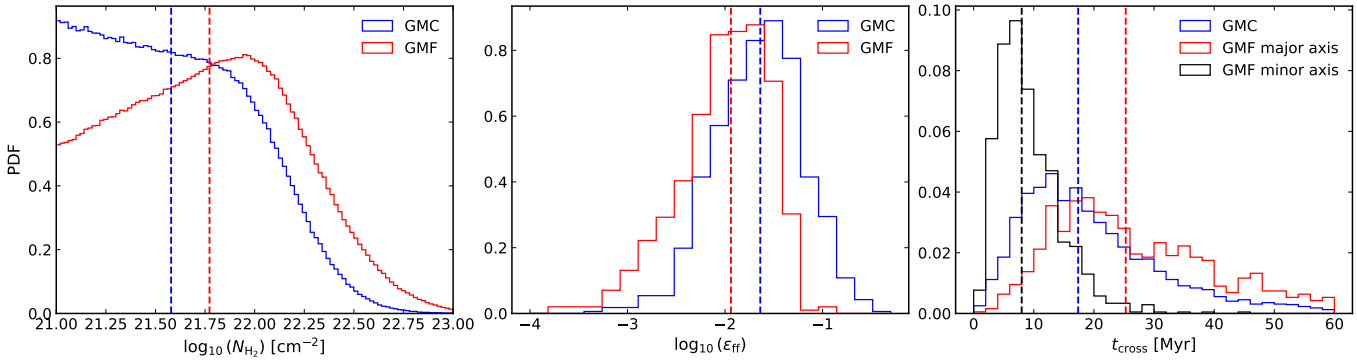

Figure 17. PDFs of physical properties for GMCs (blue) and GMFs (red). Left: H_2 column density $N_{H_2,CO}$. Middle: star formation efficiency per freefall time ϵ_{ff}. Right: crossing time t_{cross} for GMCs (blue), GMFs along the major axis (red), and GMFs along the minor axis (black). Dashed lines indicate median values for each histogram with the corresponding color.

are not a reflection of true variation in ϵ_{ff}, but rather of the limitations of observational estimators for it that integrate over times long enough that the system can evolve significantly during them.

The crossing time t_{cross} is determined for GMCs as the ratio of mean radius to velocity dispersion. For filamentary GMFs, the crossing time is anisotropic. Therefore, for each GMF contour, the crossing time is determined for both the major and minor axes with the corresponding length and velocity dispersion. The resulting PDFs are shown in the right panel of Figure 17. While the distributions differ between GMFs and GMCs, the median t_{cross} for GMCs ($\sim$17 Myr) is comparable to the filamentary lifetime t_{fil} of GMFs. This suggests that both GMCs and GMFs evolve morphologically on similar timescales.

Thus, the overall picture we form is that GMFs are similar to GMCs, but perhaps represent a slightly earlier and slightly higher column density phase of evolution.

6. Conclusion and Future Work

In this work, by conducting a synthetic CO survey of an entire simulated Milky Way–like galaxy, we provide a comprehensive statistical view of the formation and evolution of GMFs. The synthetic GMF catalog successfully reproduces the observed distributions of physical properties from certain observations, demonstrating the realism of our approach and providing a robust framework for comparing theory and observations.

Our analysis shows that GMFs typically evolve through three main stages: formation primarily driven by turbulent compression arising from galactic shear and stellar feedback, fragmentation into dense clumps induced by turbulence perturbations, and eventual dispersal driven by stellar feedback. CCCs are also frequent during their evolution, significantly reshaping their morphology and often prolonging their lifetimes. These processes highlight that GMFs are not isolated entities, but dynamically evolving structures embedded in a turbulent galactic environment.

We find that magnetized turbulence plays a dual role in GMF evolution. On one hand, it provides support against global gravitational collapse, keeping the GMFs subcritical. On the other hand, its perturbations trigger local fragmentation, leading to clump formation and subsequent star formation. As a consequence, GMFs exhibit systematically lower star formation efficiencies per freefall time compared to nonfilamentary GMCs, reflecting their turbulence-dominated nature.

The typical lifetime of GMFs as filamentary structures is $t_{fil} = 14^{+2}_{-5}$ Myr, comparable to the GMC crossing time. The molecular gas half-life, $t_{H2} \sim 7$ Myr, is similar to that of GMCs, suggesting that while GMFs are transient features, their gas properties evolve on timescales characteristic of the broader molecular cloud population.

Overall, our results demonstrate that the life cycle of GMFs is dominated by magnetized turbulence, which makes their evolution paths unique from those of normal GMCs. Due to resolution limits, our simulation cannot reproduce the thinnest GMFs observed in reality. Future high-resolution modeling is needed to comprehensively study the differences between GMFs from different catalogs and identification methodologies. We also plan to integrate MHD simulations across multiple spatial scales to develop theoretical models that can bridge 2D magnetic field observations and 3D magnetic field morphology.

Acknowledgments

We thank the anonymous referee for their valuable comments on our manuscript. Z.H., K.W., and K.S. acknowledge support from the National SKA Program of China (2025SKA0140100), the National Key R&D Program of China, and the National Natural Science Foundation of China (NSFC; No. 12573025). Z.H. acknowledges support from NSFC through grant No. 12503026 and support from Boya Fellowship at Peking University. K.W. acknowledges support from China-Chile Joint Research Fund (CCJRF No. 2211) and the Tianchi Talent Program of Xinjiang Uygur Autonomous Region. M.R.K. acknowledges support from the Australian Research Council through Laureate Fellowship FL220100020. This work was carried out with the assistance of resources from the National Computational Infrastructure (NCI Australia), an NCRIS-enabled capability supported by the Australian Government, through award jh2.

Author Contributions

Z.H. designed the simulation, performed the data analysis, and wrote most parts of this manuscript. K.W. provided supervision, comparison to observations, and editing. M.R.K. developed simulation data analysis methods and edited the manuscript. K.S. developed methods to analyze fragmentation periods.

Appendix
Projection Effects on GMF Identification

In Section 2.3, we isolate the GMF by removing foreground and background gas using two perpendicular viewing angles and project it along the minor axis of its face-on contour. However, real observations cannot always easily separate gas structures along the line of sight, and the fixed viewing angle from the Earth can hardly trace the minor axis of each GMF. To assess how these projection effects influence measured GMF properties, we perform two new sets of synthetic observations on our synthetic GMF catalog.

GMFs are typically identified in position–position–velocity (PPV) space in real observations, where gas at different physical depths is blended if it shares a similar $v_{\rm LOS}$. To mimic this, we perform synthetic observations using a methodology similar to the in-plane (edge-on) views in Section 2.3. The key difference lies in the gas particle selection: we include all gas particles within 500 pc of the GMF's center of mass, then exclude those outside the $v_{\rm LOS}$ range of the GMF identified from the original edge-on view. The 500 pc limit is chosen because gas beyond this distance exhibits a large velocity difference due to galactic rotation. We then identify GMFs from these new synthetic observations using the same criteria in Section 2.3. For each identified GMF, we measure its length, width, and mass, and compute the ratios of these values to the original ones. The 25th, 50th, and 75th percentiles of these ratios are tabulated in the first three columns of Table 2. The results show that contaminating LOS gas has a limited effect on measured lengths and widths but introduces a ∼20% uncertainty in mass measurements.

We further investigate the effects of random projection angles by repeating the synthetic observations from 100 different in-plane lines of sight, each separated by $3\overset{\circ}{.}6$, for each original GMF. We find that 34% of these lines of sight yield no GMF detection under our criteria. For lines of sight with detections, we again compute the property ratios relative to the original catalog; the percentiles are listed in the last three columns of Table 2. These values combine the effects of LOS gas and projection angle. The median length and width are affected by less than 10%, while the mass can be overestimated by about 40%.

We conclude that projection effects would cause approximately one-third of the GMFs in our simulated galaxies to be undetected in real observations. For a detected GMF, its measured length and width are likely close to the intrinsic values, but its mass may be overestimated by ∼40%. This analysis provides an initial estimate; a more detailed study using an "Earthlike" vantage point in the simulation to generate high-resolution PPV cubes for GMF and GMC identification is planned for future work.

Table 2
Percentile Statistics for GMF Property Ratios between the GMF Catalog considering Foreground and Background Gas and the Original GMF Catalog

	Edge-on Projection			Random Projection		
Property	Q1	Median	Q3	Q1	Median	Q3
Length ratio	0.99	1.04	1.27	0.91	1.04	1.38
Width ratio	0.98	1.02	1.15	0.99	1.09	1.36
Mass ratio	0.93	1.21	1.94	0.99	1.38	2.72

Note. The table shows the 25th percentile (Q1), median (50th percentile), and 75th percentile (Q3) for length, width, and mass ratios under edge-on (first three columns) and random projection angles (last three columns).

ORCID iDs

Zipeng Hu https://orcid.org/0000-0002-3758-552X
Ke Wang https://orcid.org/0000-0002-7237-3856
Mark R. Krumholz https://orcid.org/0000-0003-3893-854X
Keyun Su https://orcid.org/0009-0003-2243-7983

References

Abreu-Vicente, J., Ragan, S., Kainulainen, J., et al. 2016, A&A, 590, A131
André, P., Francesco, J. D., Ward-Thompson, D., et al. 2014, in Protostars and Planets VI, ed. H. Beuther et al. (Univ. Arizona Press), 27
André, P., Men'shchikov, A., Bontemps, S., et al. 2010, A&A, 518, L102
Arzoumanian, D., André, P., Didelon, P., et al. 2011, A&A, 529, L6
Beck, R. 2015, A&ARv, 24, 4
Bolatto, A. D., Wolfire, M., & Leroy, A. K. 2013, ARA&A, 51, 207
Chabrier, G. 2005, ASSL, 327, 41
Chandrasekhar, S., & Fermi, E. 1953, ApJ, 118, 116
Chevance, M., Kruijssen, J. M. D., Hygate, A. P. S., et al. 2020, MNRAS, 493, 2872
Chevance, M., Krumholz, M. R., McLeod, A. F., et al. 2023, ASPC, 534, 1
Colombo, D., Rosolowsky, E., Ginsburg, A., Duarte-Cabral, A., & Hughes, A. 2015, MNRAS, 454, 2067
Crutcher, R. M. 2012, ARA&A, 50, 29
da Silva, R. L., Fumagalli, M., & Krumholz, M. 2012, ApJ, 745, 145
Duarte-Cabral, A., & Dobbs, C. L. 2016, MNRAS, 458, 3667
Duarte-Cabral, A., & Dobbs, C. L. 2017, MNRAS, 470, 4261
Elmegreen, B. G., & Scalo, J. 2004, ARA&A, 42, 211
Feldmann, R., & Gnedin, N. Y. 2011, ApJL, 727, L12
Feldmann, R., Gnedin, N. Y., & Kravtsov, A. V. 2012, ApJ, 747, 124
Ferland, G. J., Korista, K. T., Verner, D. A., et al. 1998, PASP, 110, 761
Ge, Y., & Wang, K. 2022, ApJS, 259, 36
Ge, Y., Wang, K., Duarte-Cabral, A., et al. 2023, A&A, 675, A119
Glover, S. C. O., & Mac Low, M.-M. 2011, MNRAS, 412, 337
Gong, M., Ostriker, E. C., Kim, C.-G., & Kim, J.-G. 2020, ApJ, 903, 142
González-Casanova, D. F., & Lazarian, A. 2017, ApJ, 835, 41
Goodman, A. A., Alves, J., Beaumont, C. N., et al. 2014, ApJ, 797, 53
Grenier, I. A., Casandjian, J.-M., & Terrier, R. 2005, Sci, 307, 1292
Grudić, M., & Gurvich, A. 2021, JOSS, 6, 3675
Grudić, M. Y., Hopkins, P. F., Faucher-Giguère, C.-A., et al. 2018, MNRAS, 475, 3511
Hacar, A., Clark, S., Heitsch, F., et al. 2022, ASPC, 534, 153
Hacar, A., Tafalla, M., Forbrich, J., et al. 2018, A&A, 610, A77
Hanawa, T., Nakamura, F., Matsumoto, T., et al. 1993, ApJL, 404, L83
Hopkins, P. F. 2015, MNRAS, 450, 53
Hopkins, P. F. 2016, MNRAS, 462, 576
Hopkins, P. F., & Raives, M. J. 2016, MNRAS, 455, 51
Hopkins, P. F., Wetzel, A., Kereš, D., et al. 2018a, MNRAS, 477, 1578
Hopkins, P. F., Wetzel, A., Kereš, D., et al. 2018b, MNRAS, 480, 800
Hu, Z., Krumholz, M. R., Federrath, C., Pokhrel, R., & Gutermuth, R. A. 2021, MNRAS, 502, 5997
Hu, Z., Wibking, B. D., Krumholz, M. R., & Federrath, C. 2024, MNRAS, 534, 2426
Inutsuka, S.-I., & Miyama, S. M. 1992, ApJ, 388, 392
Jackson, J. M., Finn, S. C., Chambers, E. T., Rathborne, J. M., & Simon, R. 2010, ApJL, 719, L185
Jeans, J. H. 1902, RSPTA, 199, 1
Jeffreson, S. M. R., Semenov, V. A., & Krumholz, M. R. 2024, MNRAS, 527, 7093
Jiang, Y., Chen, X., Zheng, S., et al. 2025, ApJS, 276, 27
Jow, D. L., Hill, R., Scott, D., et al. 2018, MNRAS, 474, 1018
Kim, J.-h., Agertz, O., Teyssier, R., et al. 2016, ApJ, 833, 202
Klessen, R. S., & Glover, S. C. O. 2016, SAAS, 43, 85
Koch, E. W., & Rosolowsky, E. W. 2015, MNRAS, 452, 3435
Kruijssen, J. M. D., Schruba, A., Chevance, M., et al. 2019, Natur, 569, 519
Krumholz, M. R. 2014, MNRAS, 437, 1662
Krumholz, M. R., Fumagalli, M., da Silva, R. L., Rendahl, T., & Parra, J. 2015, MNRAS, 452, 1447
Krumholz, M. R., McKee, C. F., & Bland-Hawthorn, J. 2019, ARA&A, 57, 227
Larson, R. B. 1981, MNRAS, 194, 809
Li, C., Qiu, K., Hu, B., & Cao, Y. 2021, ApJL, 918, L2

Nagasawa, M. 1987, PThPh, 77, 635
Nakamura, F., Hanawa, T., & Nakano, T. 1993, PASJ, 45, 551
Narayanan, D., Krumholz, M., Ostriker, E. C., & Hernquist, L. 2011, MNRAS, 418, 664
Narayanan, D., Krumholz, M. R., Ostriker, E. C., & Hernquist, L. 2012, MNRAS, 421, 3127
Ntormousi, E. 2018, A&A, 619, L5
Paré, D. M., Lang, C. C., & Morris, M. R. 2024, ApJ, 974, 200
Pillsworth, R., Roscoe, E., Pudritz, R. E., & Koch, E. W. 2025, ApJ, 987, 20
Planck Collaboration, Ade, P. A. R., Aghanim, N., et al. 2016, A&A, 586, A138
Ragan, S. E., Henning, T., Tackenberg, J., et al. 2014, A&A, 568, A73
Ramambason, L., Lebouteiller, V., Madden, S. C., et al. 2024, A&A, 681, A14
Robinson, H., Wadsley, J., Sellwood, J. A., & Pudritz, R. E. 2025, ApJ, 989, 205
Robitaille, T., Rice, T., Beaumont, C., et al., 2019 astrodendro: Astronomical data dendrogram creator, Astrophysics Source Code Library, ascl:1907.016
Shetty, R., Glover, S. C., Dullemond, C. P., & Klessen, R. S. 2011a, MNRAS, 412, 1686
Shetty, R., Glover, S. C., Dullemond, C. P., et al. 2011b, MNRAS, 415, 3253
Smith, B. D., Bryan, G. L., Glover, S. C. O., et al. 2017, MNRAS, 466, 2217
Soler, J. D., & Hennebelle, P. 2017, A&A, 607, A2
Soler, J. D., Hennebelle, P., Martin, P. G., et al. 2013, ApJ, 774, 128
Solomon, P., & Vanden Bout, P. 2005, ARA&A, 43, 677
Sousbie, T., Pichon, C., & Kawahara, H. 2011, MNRAS, 414, 384
Temim, T., Laming, J. M., Kavanagh, P. J., et al. 2024, ApJL, 968, L18
Wang, K., & Ge, Y., 2021 MST: Minimum Spanning Tree algorithm for identifying large-scale filaments, Astrophysics Source Code Library, ascl:2102.002
Wang, K., Ge, Y., & Baug, T. 2024, A&A, 686, L11
Wang, K., Testi, L., Burkert, A., et al. 2016, ApJS, 226, 9
Wang, K., Testi, L., Ginsburg, A., et al. 2015, MNRAS, 450, 4043
Xie, Y.-H., & Li, G.-X. 2025, ApJL, 983, L21
Yuen, K. H., & Lazarian, A. 2017, ApJL, 837, L24
Zhao, B., Pudritz, R. E., Pillsworth, R., Robinson, H., & Wadsley, J. 2024, ApJ, 974, 240
Zucker, C., Battersby, C., & Goodman, A. 2015, ApJ, 815, 23
Zucker, C., Battersby, C., & Goodman, A. 2018, ApJ, 864, 153
Zucker, C., & Chen, H. H.-H. 2018, ApJ, 864, 152
Zucker, C., Smith, R., & Goodman, A. 2019, ApJ, 887, 186